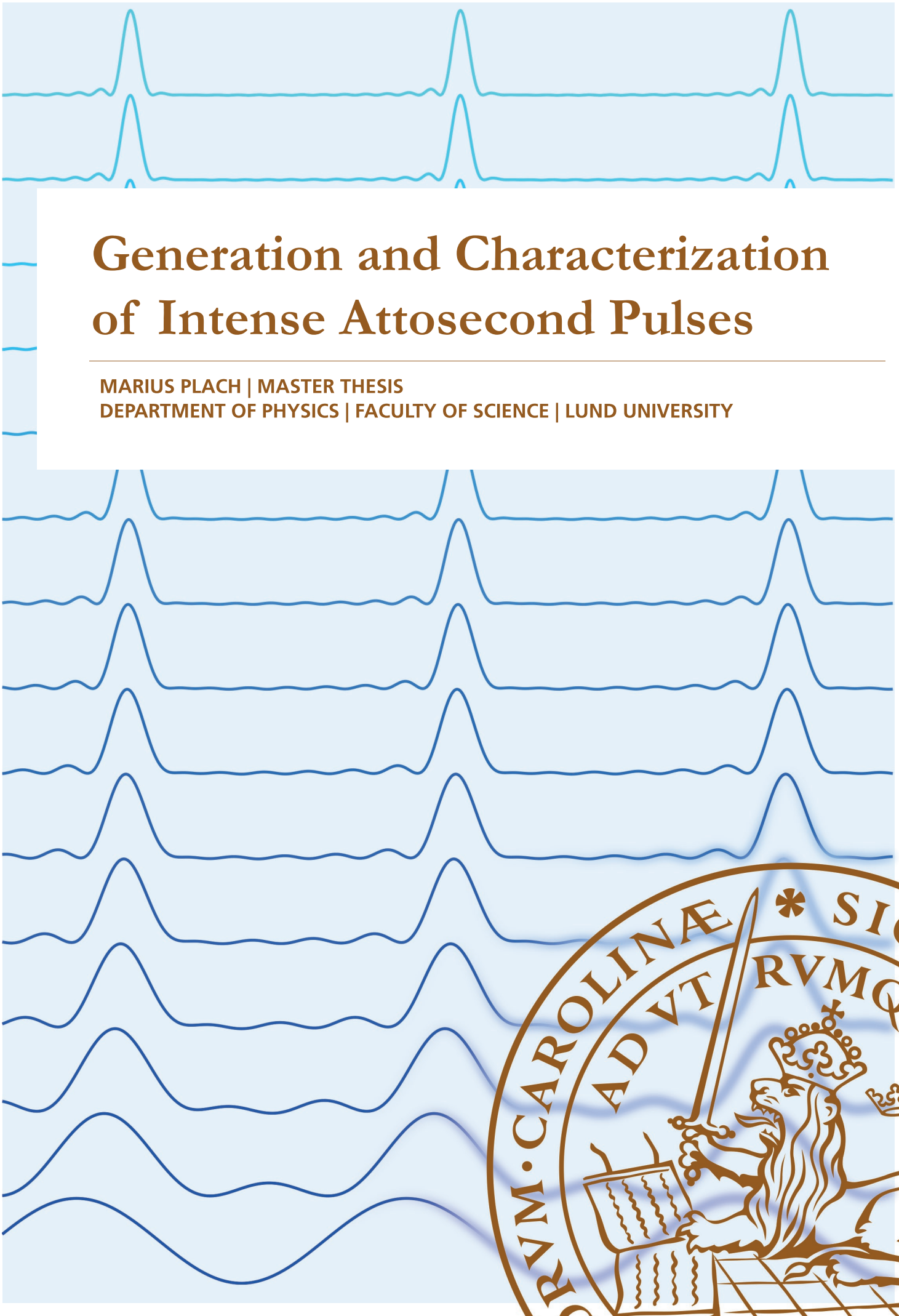

Generation and Characterization of Intense Attosecond Pulses

MARIUS PLACH | MASTER THESIS
DEPARTMENT OF PHYSICS | FACULTY OF SCIENCE | LUND UNIVERSITY

This Master thesis work took place between April 2019 and May 2020 (duration 12 months) at the Atomic Physics division of the Department of Physics at the Lund University, and was submitted on 11th May 2020. The examination took place on the 25th May 2020.

Supervisor: Professor Per Johnsson
Co-supervisor: Jasper Peschel
Examiner: Senior Lecturer Dr. Claudio Verdozzi
Co-examiner: David Busto

Abstract

Research on ultrafast dynamics in atoms and molecules requires short pulses. In order to resolve processes taking place on a femtosecond timescale sufficiently, these pulses require a duration on the attosecond time scale.
This thesis is about the generation of such attosecond pulses via high harmonic generation (HHG) in argon gas by a terawatt infrared (IR) laser source. The pulses are applied in a pump-probe principle on two different noble gases, helium and neon. Reconstruction of Attosecond Beating By Interference of Two-photon Transition (RABBIT) is performed to characterize the relative emission time delay between harmonics, and to reconstruct the temporal domain of the attosecond pulse. Methods used for analyzing and improving the data extraction are introduced. Particularly the angle-resolved analysis gives unique insights into the ionization dynamics.

Contents

List of abbreviations

ATI Above Threshold Ionization

APT Attosecond Pulse Train

BBO Barium borate BaB_2O_4

CPA Chirped Pulse Amplification

CCD Charge-coupled Device

DM deformable mirror

DVMIS Double Sided Velocity Map Imaging Spectrometer

XUV eXtreme Ultra Violet

FWHM Full Width at Half Maximum

GDD Group Delay Dispersion

HHG high-order harmonic generation

IR Infrared

LLC Lund Laser Center

MCP Micro-Channel Plate

MPI Multi-Photon ionization

RABBIT Reconstruction of Attosecond Beating By Interference of Two-photon Transition

SHG Second Harmonic Generation

VMI Velocity Map Imaging

WFS Wavefront sensor

1 Introduction

This thesis is about the theoretical and experimental requirements to generate intense attosecond pulses and the analysis and characterization when they are applied. Attosecond pulses are light pulses with an ultra-short time duration in the attosecond range (10^{-18} s) and amongst the shortest phenomena we can artificially create nowadays. The need for attosecond pulse sources is due to the investigation of fundamental processes of ultra-fast atomic and molecular dynamics such as ionization or excitation, or more general charge migration. These experiments take place in the non-linear regime and thus require high intensity. The sources as we use today could not exist without the invention of the first laser in 1960 [1]. This event laid the fundament of the research field photonics since high intense light sources became suddenly available. This lead to the first demonstration of a non-linear effect, the Second Harmonic Generation (SHG) only one year later in 1961 [2]. Around that time, significant effort on the theoretical explanation of the interaction between strong laser fields and atomic potentials had been contributed by Keldysh et al. [3]. After mode locking and Q-switching lead to a significant growth in the available maximal laser intensity, the plateau of this development was reached for the time being. The discovery of Chirped Pulse Amplification (CPA) in 1985 was the next breakthrough in history towards higher laser intensities, which still goes on until this day [4]. The theory of the generation of high harmonics as a result of the interaction of atoms with strong laser fields had been stated in 1994 [5]. In the same year, the first results at the high-power laser facility in Lund had been obtained [6]. The Lund Terawatt Laser System, as one of the first ones ever, generated pulses with a duration of about 150 fs at this time. The theory of generating attosecond pulses using high harmonics produced with femtosecond lasers had been stated in 1996 [7]. From then it took another five years until attosecond pulses were discovered with a pulse duration of 250 as, using the method of Reconstruction of Attosecond Beating By Interference of Two-photon Transition (RABBIT)[8]. Nowadays, we are able to generate attosecond pulses with a duration below 100 as on a daily basis. The shortest pulses based on high-order harmonic generation (HHG) have a duration of only 43 as [9]. One focus of today's research is the investigation of angle-resolved phenomena at the interaction of light and matter [10] [11] [12]. In this work, we undergo the analysis process of attosecond pulses to verify the reliability of the setup. Then, a method is introduced to improve the single image quality of the Velocity Map Imaging (VMI) maps and to enable the extraction of information from the data with an increase in detail.

1.1 Motivation behind this thesis

Natural science, particularly physics is stating rules describing our environment, and often discovers explanations for things the human brain cannot imagine. I have been jealous of astrophysicists as they are talking about such things on a daily basis, like galaxies in light years distance,

black holes with infinite mass or dark matter which must be everywhere but is nowhere. This fascination is driven to the edge where contrary phenomena meet each other and macroscopic large numbers hit on microscopic small scales. One can also find a piece of these two worlds in our research. We use one of Scandinavia's strongest lasers in the terawatt range to investigate phenomena taking place in the shortest time frame of attoseconds. The experiment we operate spans over two large rooms and is occupying probably six times the place I lived during this thesis work, only to investigate what is happening in a volume of about 15 square-micrometer. Thus, my motivation is driven by reaching the line where complex things are explained and rules are formed enabling to satisfy the need in all of us to understand the unimaginable.

1.2 Thesis outline

Chapter 2 provides a theoretical background of the generation of high harmonics and how attosecond pulses are generated and characterized. Chapter 3 expands on the experiment, the Terawatt Laser System as the source of femtosecond laser pulses and the Intense XUV Beamline where the pulses are applied. Chapter 4 describes the method to analyze the measurements in Helium and Neon as a target gas. The results of this thesis work are presented and discussed. Chapter 5 concludes the thesis by a summary and draws an outlook on what is going to follow this work.

2 Theory

Conducting research on ultra-fast charge dynamics of small quantum systems requires to know the circumstances (energy, contributing processes, time frame) under which the ionization process occurs. A short temporal resolution of the measurement is necessary to resolve the observations sufficiently high. The availability of light sources based on HHG sets this time frame to an attosecond scale, giving this field of research its name *attosecond science*. The first part of this chapter (Section 2.1) introduces different ionization processes of atoms in strong laser fields and a way to categorize them in order to meet predictions about which process is likely to happen at the corresponding strong-field regime. One of these regimes, the so-called tunneling regime is supporting high harmonic generation. The occurrence of equally distanced high-order harmonic spectral peaks (as a frequency comb) in the eXtreme Ultra Violet (XUV) range is explained by the Three-Step Model in Section 2.2. The temporal resolution of such a frequency comb is of major interest. Following this, the generation of pulses with duration less than $\tau = 100\,\mathrm{as}$ is analytically derived in Section 2.3 as an interference phenomenon. The effect of different phase contributions on the temporal profile is discussed. Finally, the RABBIT technique is introduced as a means to experimentally determine the phase, characterize the Attosecond Pulse Train (APT) and investigate ionization dynamics in Section 2.4.

2.1 Strong-field processes in atomic gases

In an atom, an applied electric field of sufficient strength alters the binding potential of the electron. The effective potential V_{Eff} is formed by superimposing the Coulomb potential for an electron with charge e and the electric field $E(t)$ of a laser that oscillates periodically with time:

$$V_{\mathrm{Eff}} = \underbrace{-\frac{e^2}{4\pi\varepsilon_0|z|}}_{\text{Coulomb potential}} + \underbrace{eE_0\sin(\omega_0 t)z}_{\text{Laser field potential}} \quad , \tag{2.1}$$

with the vacuum permitivity ε_0, the amplitude E_0 and the frequency ω_0 of the electric field. Figure 2.1 shows the field-free Coulomb potential, the time dependent electric laser field as well as the superposition of both contributions as the effective potential V_{Eff}.

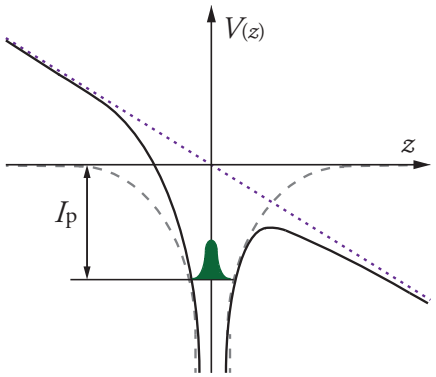

Figure 2.1: Electron in a Coulomb potential (grey-dashed), laser field (purple-dotted) and the effective potential in a field environment (black). The laser field which oscillates with time is shown at its highest field strength. The ionization potential I_p is the energy required to remove the electron from the field-free Coulomb potential.

It is useful to define the ponderomotive potential U_p with the electron mass m_e:

$$U_p = \frac{e^2E_0^2}{4m_e\omega_0^2} \, . \tag{2.2}$$

The ponderomotive potential is the mean energy of the electron in the presence of a strong oscillating field that superimposes with the core potential. Depending on the laser frequency ω_0 and intensity $I \propto |E_0|^2$, the electron faces different ionization processes which can be divided into three regimes, the multi-photon ionization, tunnel-ionization and the over-the-barrier ionization regime. These fundamental strong field processes are depicted in Figure 2.2. The case where several photons are able to ionize the electron is called Multi-Photon ionization (MPI) regime. Increasing the ponderomotive energy (turning to lower frequency or stronger fields $> 1\,\mathrm{TW/cm^2}$) one crosses the Above Threshold Ionization (ATI) regime. This is the special case of MPI where more photons are absorbed than needed to overcome the ionization barrier. The electron is released with additional kinetic energy. Experiments have shown the feasibility of MPI/ATI in xenon with a $\lambda = 1053\,\mathrm{nm}$ Nd:glass laser and field intensities I of a few $\approx 10^{13}\,\mathrm{W/cm^2}$ [13]. When the ponderomotive energy exceeds the energy of the Coulomb-barrier (low frequencies and

strong fields), the electron is likely to tunnel the potential. For Ti-Sapphire laser ($\lambda = 800\,\mathrm{nm}$) this regime spans approximately from $I = 10^{14}$ to $10^{15}\,\mathrm{W/cm^2}$. Even stronger fields cause over-the-barrier ionization, also called barrier suppression-regime. In this case the laser intensity is high enough to distort the effective potential so much that the electron can escape. This effect could be proven with different noble gases using a $\lambda = 1053\,\mathrm{nm}$ Nd:glass laser and intensities between $I = 10^{14}\,\mathrm{W/cm^2}$ and $10^{16}\,\mathrm{W/cm^2}$ [14].

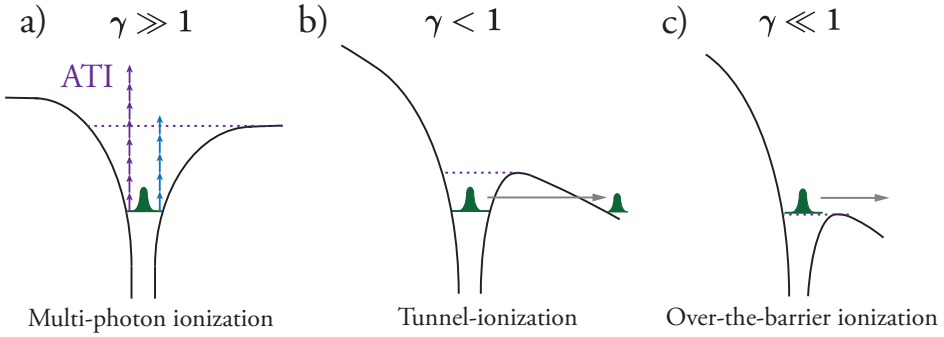

Figure 2.2: Effective potential the electron is facing at different ionization regimes and the associated ionization processes. Figure a) sketches multi-photon ionization and above-threshold ionization. Figure b) shows the tunnel-ionization regime. In Figure c) the potential is sufficiently distorted allowing the electron to ionize unobstructively.

Keldysh introduced the adiabaticity parameter γ in 1964 as a means to indicate which ionization process is likely to happen [3]. Hereby, the strong field frequency must be lower than the ionization potential $\hbar\omega_0 > I_\mathrm{p}$ to avoid single photon ionization. The Keldysh parameter is expressed as follows:

$$\gamma = \omega_0 \frac{\sqrt{2 m_\mathrm{e} I_\mathrm{p}}}{e E_0}\,, \tag{2.3}$$

with the electron mass m_e and the ionization potential I_p. The Keldysh parameter can also be expressed in terms of U_p:

$$\gamma = \sqrt{\frac{I_\mathrm{p}}{2U_\mathrm{p}}}\,. \tag{2.4}$$

Table 2.1 gives an overview of the different ionization regimes and their corresponding Keldysh parameter. The different Keldysh regimes are also marked in the upper part of Figure 2.2. The

Table 2.1: Different ionization regimes, depending on the Keldysh-parameter respectively the relation between ionization potential, ponderomotive energy and photon energy.

Ionization regime	Keldysh parameter	Ponderomotive
Multi-photon ionization (MPI)	$\gamma \gg 1$	$I_p > \hbar\omega_0 \gg U_p$
Above-threshold ionization (ATI)		$I_p > U_p > \hbar\omega_0$
Tunnel ionization (TI)	$\gamma < 1$	$U_p > I_p > \hbar\omega_0$
Over-the-barrier ionization	$\gamma \ll 1$	$U_p \gg I_p > \hbar\omega_0$

Keldysh parameter cannot be considered as a strict categorization but rather a rough assessment on which process is likely to happen at what laser parameters.

2.2 The Three-Step Model

We consider the tunneling regime with low frequency ω_0 and strong fields E_0 ($\gamma < 1$). The semi-classical three-step model describes the generation of high order harmonics on the base of three consecutive steps; tunnel-ionization, acceleration and recombination [13] [15]. The atomic Coulomb potential is distorted in such a way that there is a likelihood that the electron tunnels through the barrier (fig. 2.3 step I). It gains kinetic energy as it is driven away by the field. However, it is turning direction backwards towards the atom when the field changes its sign (fig. 2.3 step II). The trajectory of the electron describes an arc. It recombines with its parent atom and releases its gained kinetic energy in form of a photon $\hbar\omega$ (fig. 2.3 step III). The amount of energy depends on the ionization time t_i with respect to the field oscillation and the ponderomotive potential.

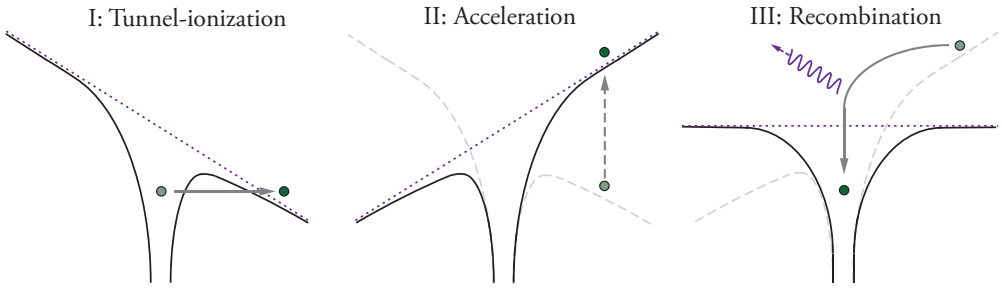

Figure 2.3: Visualization of the three-step model comprising tunnel-ionization (I), acceleration (II) and recombination (III) under emission of a photon. The effective potential (black) is the Coulomb-potential distorted by the time-dependent laser field (purple-dashed). The three graphics illustrate the succession of events in time (from left to right).

The trajectory of a tunneled electron is now classically described. The laser field acting on the charge is of the form $E(t) = E_0 \sin(\omega_0 t)$ with amplitude E_0, frequency ω_0 and t denotes time. The following differential equation is derived from the Lorentz force:

$$m_\mathrm{e}\ddot{z} = -\mathrm{e}E(t)\ , \tag{2.5}$$

with the electron charge e, and its mass m_e. The acceleration is given by $\ddot{z}$. A defined integration from the ionization time t_i (the time when the electron has just tunneled through the barrier) to t gives the velocity $\dot{z}(t)$:

$$\dot{z}(t) = \frac{\mathrm{e}E_0}{m_\mathrm{e}\omega_0}\left[\cos\omega_0 t - \cos\omega_0 t_\mathrm{i}\right] \tag{2.6}$$

A second integration and application of the initial conditions $\dot{z}(t_\mathrm{i}) = 0$ and $z(t_\mathrm{i}) = 0$ leads to

the trajectory

$$z(t) = \frac{eE_0}{m_e\omega_0^2}\left[\sin(\omega_0 t) - \sin(\omega_0 t_i) - \omega_0 (t - t_i)\cos(\omega_0 t_i)\right] \ . \tag{2.7}$$

The electron is able to recombine with its parent atom at the recombination time t_r for which Equation (2.7) has a zero-crossing $z(t_r) = 0$. This can be solved for every t_i. Figure 2.4 a) shows for what trajectories recombination can occur (colored). For the other ionization times the electron is driven away from its atom (grey-dashed line). However, there is still a probability that the electron just passes through the potential without recombination, undergoing another oscillation to recombine at a later cycle.

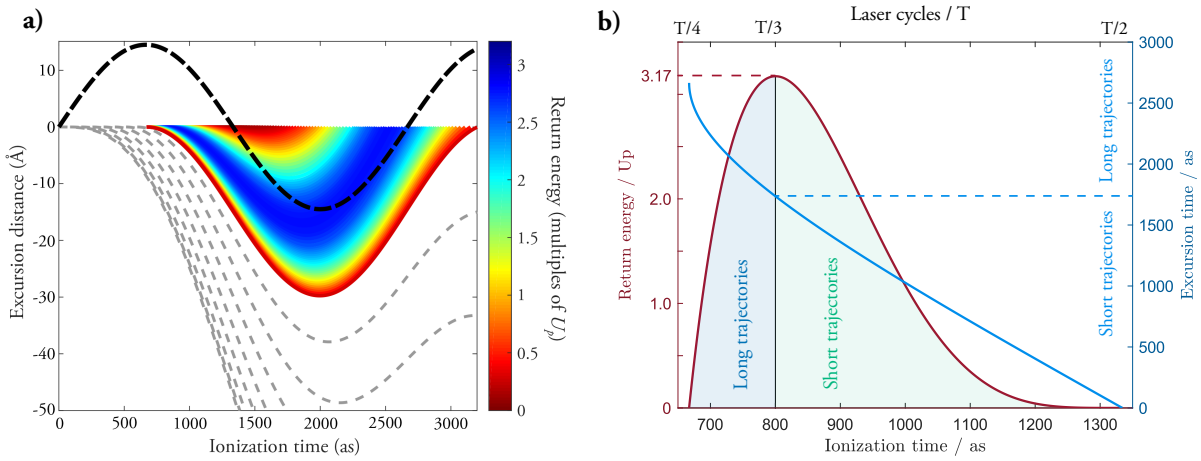

Figure 2.4: a) Trajectories of the electron depending on the ionization time t_i for which recombination is possible (coloured), as well as trajectories for which the electron is driven away (grey-dashed). The process takes place every half laser cycle (black dashed). Figure a) taken from [16]. b) Electron return energy (red, left axis) and excursion time of a returning electron (blue, right axis) depending on its ionization time t_i. The parameters used for the calculations match those in the experiment with $I = 3.3{\cdot}10^{14}\,\mathrm{W/cm^2}$ and $\lambda = 800\,\mathrm{nm}$.

The time the atom is ionized t_i determines the recombination time t_r and thus the kinetic energy the electron will have gained from the laser field when returning. The excursion time t_e is the difference between recombination time and ionization time $t_e = t_r - t_i$. Electrons which are ionized in the first quarter of a laser cycle ($t_i < T/4$) are driven away by the field and do not return. The electron excursion time is assigned to either long or short trajectories. Electrons ionized early (between $T/4 < t_i < T/3$) have a long excursion time and are referred to the long trajectories. They are represented by the left side of the peak in the return energy plot of Figure 2.4 b). Short trajectory electrons are ionized later in the laser cycle ($T/3 < t_i < T/2$). Hence, they are returning faster since the accelerating laser field is already about to decrease rapidly when they are released. The energy E_{ph} of the photon emitted at recombination consists of the kinetic energy E_{kin} plus the ionization potential:

$$E_{ph} = E_{Kin} + I_p = \frac{1}{2}\, m_e(\dot{z}(t))^2 + I_p \ . \tag{2.8}$$

Further investigation of function (2.7) reveals the maximal return-energy to be $E_{max} = 3.17U_p$.

Since the electron will overcome the ionization potential when recombining, the maximal possible photon energy is

$$E_{\mathrm{ph}} = 3.17U_{\mathrm{p}} + I_{\mathrm{p}} \, . \tag{2.9}$$

This is also denoted as the cut-off energy, and was first empirically discovered by Krause et al. [17]. This process repeats every half laser cycle. As a result, a set of harmonics is generated with an intensity distribution as shown in Figure 2.5. The spectrum contains only odd order harmonics. This is due to the destructive interference of waves which are phase-shifted by π between two consecutive laser half cycles.

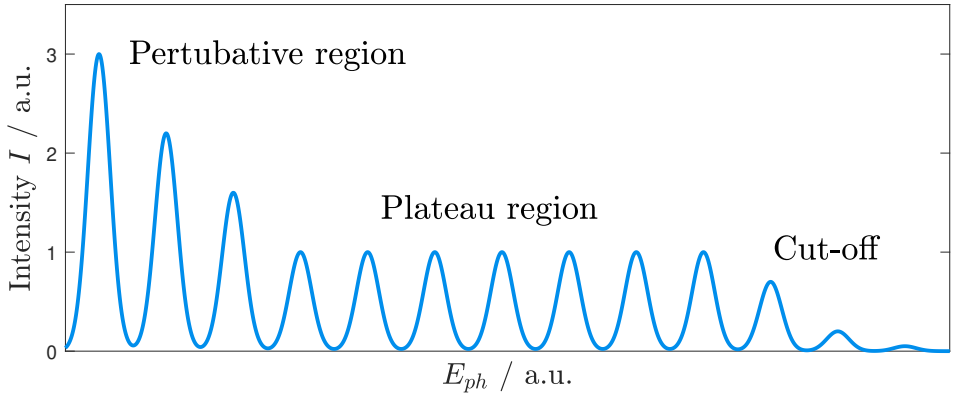

Figure 2.5: Characteristic intensity distribution of the pulses created by HHG. This frequency comb consists of odd-order harmonics due to the destructive interference of photons from consecutive laser half-cycles which are phase shifted by π.

The decline of the intensity in the pertubative region is due to a lower probability of q-photon-absorption events the higher the q^{th} harmonic gets. The cut-off as derived in Equation (2.9) causes an abrupt decrease of the intensity. The absolute values depend on the gas used for generation, phase matching and the fundamental laser wavelength. The photons are usually in the XUV range which requires vacuum for propagation, since air is highly absorbent at these energies.

2.3 Attosecond pulse generation

So far, we only regarded the frequency domain of the HHG. The spectra can generate pulses with duration in the attosecond range if the phases of the contributing harmonics match properly. Therefore, we consider harmonic order phase matching as key for attosecond pulse generation and investigate the temporal domain of the frequency comb in this part, as this is of major importance for the application. We define the harmonics as a sum of their complex amplitudes between the 11th and 39th order. The high-order phase contribution is explicitly neglected here,

but will be considered later:

$$E_q = E_{11} + E_{13} + ... + E_{39} = \sum_{q\,=\,11}^{39} e^{iq\omega_0 t} \;;\; q \text{ odd} \tag{2.10}$$

$$\Leftrightarrow E_q = \sum_{q\,=\,0}^{14} e^{11i\omega_0 t} \cdot e^{2iq\omega_0 t} = e^{11i\omega_0 t} \underbrace{\sum_{q\,=\,0}^{14} e^{2iq\omega_0 t}}_{\text{geometric series}} \;;\; q \in \mathbb{Z}^+$$

$$\Leftrightarrow E_q = e^{11i\omega_0 t} \frac{1 - e^{15(2i\omega_0 t)}}{1 - e^{2i\omega_0 t}} = e^{11i\omega_0 t} \frac{e^{15i\omega_0 t}}{e^{i\omega_0 t}} \left(\frac{e^{-15i\omega_0 t} - e^{15i\omega_0 t}}{e^{-i\omega_0 t} - e^{i\omega_0 t}} \right)$$

$$\Leftrightarrow E_q = e^{25i\omega_0 t} \left(\frac{\sin(15\omega_0 t)}{\sin(\omega_0 t)} \right). \tag{2.11}$$

The intensity is defined as the absolute value of the electrical field squared. The complex prefactor vanishes:

$$I(t) \propto \left| E_q \right|^2 = \left| \frac{\sin(15\omega_0 t)}{\sin(\omega_0 t)} \right|^2 . \tag{2.12}$$

The total number of harmonics in this example is 15, but can be equally replaced with a finite integer m. Equation 2.12 does not only remind of a sinc function, but also shows the same curve behaviour as it forms a peak in the time domain. Figure 2.6 (dark blue) plots the intensity $I(t)$ for a fundamental laser wavelength of $\lambda = 800\,\text{nm}$ and a sum of 15 high harmonics.

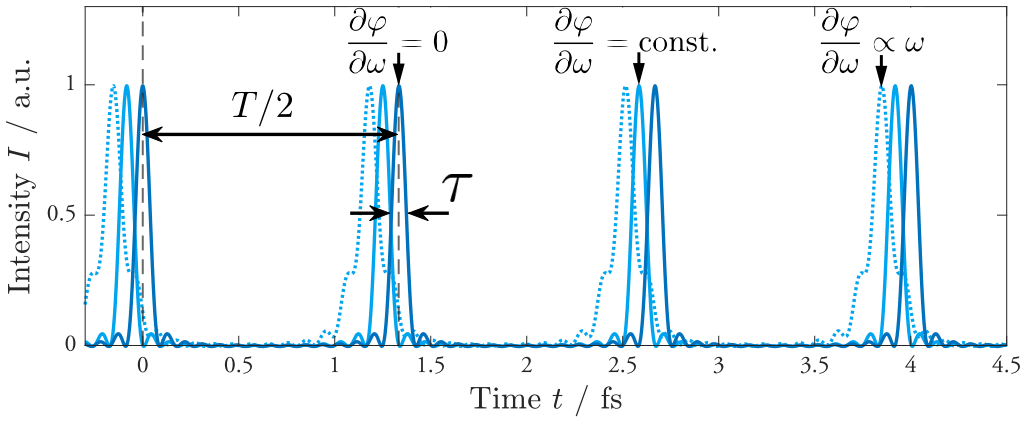

Figure 2.6: Visualization of Equation (2.12) normalized (dark blue). The bright blue line represents the temporal profile with a constant frequency-dependent phase difference between two consecutive harmonics. This leads to a constant group delay (Equation (2.16)) while the pulse train duration τ remains. The bright blue dashed line contains a quadratic phase difference, leading to a broadening.

The denominator in Equation (2.12) determines the repetition time, as a peak is present for every multiple integer n of the argument of the sinus function:

$$\omega_0 t = n\pi \Longleftrightarrow t = n\,\frac{\pi}{\omega_0} \;. \tag{2.13}$$

For the laser period $T_{\text{Laser}} = 2\pi/\omega_0$ there is $n = 2$ peaks per laser cycle which gives the difference

T/2 between consecutive peaks. This is well in accordance to the three-step model where emission occurs every half cycle. The duration of the individual pulses in the train τ is defined by the Full Width at Half Maximum (FWHM). Both parameters are also marked in Figure 2.6. In this example the pulse train duration is determined to:

$$\tau \approx 80\,\text{as} \quad . \tag{2.14}$$

This explains the generation of ultra-short pulse trains with attosecond duration as an interference process of a set of equidistant peaks. However, the derivation does not consider any harmonic order phase contribution as the harmonics are assumed to be perfectly synchronized with respect to each other. This is not correct since Figure 2.4 reveals already clearly that HHG is caused by recombination of electrons with different energies and at different times. This time-delay will induce an intrinsic chirp on the harmonics meaning a phase contribution depending on the order of the high harmonic. The intensity of the sum of harmonics considering a phase contribution is defined as

$$I(t) = \left| \sum_{q \text{ odd}} A_q e^{i(q\omega_0 t + \varphi_q)} \right|^2 \quad . \tag{2.15}$$

This phase contribution changes the temporal shape of the attosecond pulse. The group delay τ_g is introduced as the first order derivation of the spectral phase:

$$\tau_\text{g} = \frac{\partial \varphi_q}{\partial \omega} \quad . \tag{2.16}$$

Another useful expression is the Group Delay Dispersion (GDD). It is defined as the derivative of the group delay, or second order derivation of the phase:

$$\text{D}_2(\omega) = \frac{\partial \tau_\text{g}}{\partial \omega} = \frac{\partial^2 \varphi_q}{\partial \omega^2} \quad . \tag{2.17}$$

A nonzero GDD means a chirping of the pulse. A linear frequency dependence of the phase leads to a constant group delay $\frac{\partial \varphi_q}{\partial \omega} = \text{constant}$. This case is drawn in Figure 2.6 for the set of harmonics in Equation (2.10) with a linear phase-shift spreading from 0 to 2 radian over all harmonics. This delays the pulses but does not affect the duration since the group delay τ_g is constant but the group delay dispersion $\text{D}_2(\omega)$ equals zero. Following this, a phase shift spreading from 0 to 3π rad with a quadratic frequency dependency is plotted. In this case, the GDD is not equal to zero. An attosecond chirp is induced varying the group delay over the frequency ω and broadening the temporal profile. In the following example, the intensity is treated as a sum of harmonics, analogue to Equation (2.15). Furthermore, a phase shift φ_q and an arbitrary amplitude A_q is added to any harmonic. Only three harmonics, 13, 15 and 17 are considered, but the calculation can be performed analogue any number of harmonics:

$$I(t) = \left| A_{13} e^{i(13\omega_0 t + \varphi_{13})} + A_{15} e^{i(15\omega_0 t + \varphi_{15})} + A_{17} e^{i(17\omega_0 t + \varphi_{17})} \right|^2 \quad .$$

The phase contribution of the highest harmonic $e^{i\varphi_{17}}$ is extracted:

$$\Longleftrightarrow I(t) = \left| e^{i\varphi_{17}}[A_{13}e^{i(13\omega_0 t+\varphi_{13}-\varphi_{17})} + A_{15}e^{i(15\omega_0 t+\varphi_{15}-\varphi_{17})} + A_{17}e^{i(17\omega_0 t)}] \right|^2$$

$$\Longleftrightarrow I(t) = \left| \underbrace{e^{i\varphi_{17}}}_{1}[A_{13}e^{i(13\omega_0 t+\varphi_{13}-\varphi_{17}+\varphi_{15}-\varphi_{15})} + A_{15}e^{i(15\omega_0 t-\Delta\varphi_{17-15})} + A_{17}e^{i(17\omega_0 t)}] \right|^2$$

φ_{17} is an arbitrary delay, added to all harmonics and can be set to zero:

$$\Longleftrightarrow I(t) = \left| A_{13}e^{i(13\omega_0 t-\Delta\varphi_{17-15}-\Delta\varphi_{15-13})} + A_{15}e^{i(15\omega_0 t-\Delta\varphi_{17-15})} + A_{17}e^{i(17\omega_0 t)} \right|^2 \tag{2.18}$$

For every additional considered harmonic, there is another phase difference contribution in the lower terms. To reconstruct the temporal domain of the attosecond pulse, one needs to know the phase shift $\Delta\varphi$ between consecutive harmonics and their relative intensity. The latter can be determined with a spectrometer but determining the phase differences $\Delta\varphi$ is rather complicated. RABBIT is a method for doing this.

2.4 The RABBIT technique

As mentioned in the previous section, a crucial challenge of attosecond physics is the detection of such short pulses. There is no sensor (photodiode or equivalent) with sufficient time resolution. RABBIT is a pump-probe technique for characterizing attosecond pulses. In this method, the HHG radiation is targeted on an atomic or molecular gas. The interaction between the high harmonic attosecond pulses and atoms with ionization potential I_p releases photoelectrons with discrete kinetic energies equal to $E_\mathrm{Kin} = (2q+1)\hbar\omega_0 - I_\mathrm{p}$ with q the high harmonic order. The presence of the fundamental Infrared (IR) laser field generating the high harmonics causes two-color two-photon transitions generating additional sidebands in the photoelectron spectrum. Following [8], we consider a weak field regime where only single IR photons are absorbed. Each harmonic contributes to only one single sideband each side. Each sideband has two contributions: One from the q-th harmonic plus an IR photon, as well as one from the $(q+2)$-th harmonic minus one IR-photon. Figure 2.7 illustrates the schematic result of this process. One can see strong peaks assigned to the odd harmonics (15ω, 17ω, 19ω). In addition, there are sidebands between two peaks, corresponding to even multiples of the IR-frequency. Due to the two interference contributions, the sideband signal amplitude oscillates with [8]:

$$A_\mathrm{SB} \propto \cos\left[2\omega_0\tau - \Delta\varphi_\mathrm{atto} - \Delta\varphi_\mathrm{atomic}\right] \quad , \tag{2.19}$$

using τ the induced delay between the attosecond pulse train and the IR laser field and $\Delta\varphi_\mathrm{atto}$ the phase difference between harmonics of the attosecond pulse-train corresponding to the so-called attochirp [18]. This quantity is needed for all contributing sidebands to reconstruct the temporal domain of the attosecond pulse. $\Delta\varphi_\mathrm{atomic}$ is the accumulated phase difference between absorption and emission of an IR photon and the ionization phase. Delaying the IR field with respect to the harmonics, using an optical delay line, changes τ. The intensity profile recorded

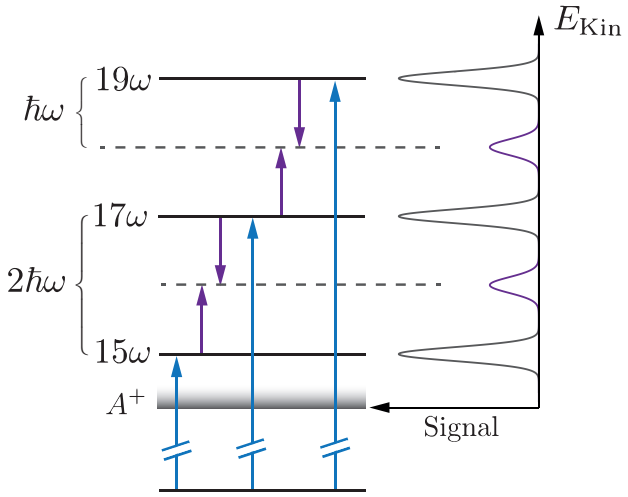

Figure 2.7: Sideband generation due to two-photon processes. The high harmonics (blue) receive or lose the energy of an IR-photon (purple) leading to sideband contributions coming from two harmonics.

for a set of delays τ is then the RABBIT-scan. However, the analysis of a RABBIT-scans returns only the relative phase $\Delta\varphi_{\mathrm{SB}}$. Both phase contributions can also be expressed as group delay times:

$$\Delta\varphi_{\mathrm{SB}} = \Delta\varphi_{\mathrm{atto}} + \Delta\varphi_{\mathrm{atomic}} = 2\omega_0 \left(\tau_{\mathrm{atto}} + \tau_{\mathrm{atomic}}\right) \tag{2.20}$$

It is rather difficult to determine the delay times separately from each other since the processes cannot be triggered independently from each other. However, the atomic phase term is often a small contribution [18]. Being only interested in the harmonic emission time delay τ_{atto} this contribution can often be neglected:

$$\tau_{\mathrm{atto}} = \frac{\partial\varphi}{\partial\omega} = \frac{\Delta\varphi_{\mathrm{atto}}}{2\omega_0} \approx \frac{\Delta\varphi_{\mathrm{SB}}}{2\omega_0} \tag{2.21}$$

Research had been driven on the investigation of the atomic contribution since this value contains information about the ionization process itself [19]. Recent studies revealed that these processes can be anisotropic and research focuses now on conducting angular resolved analysis of the phenomenon [11].

3 Experimental approach

The experimental setup of this thesis work is located at the Lund Laser Center (LLC) and consists of two parts, the Terawatt Laser System and the Intense XUV Beamline. The Terawatt Laser System (Section 3.1) produces the high-energy laser pulses which are then used for experiments in the beamline part. The beam is propagating under vacuum between the two parts which are located in different rooms. It makes sense to further subdivide the Intense XUV Beamline into two parts; the generation part and the application part. Figure 3.1 shows the beamline as it has been used to perform the RABBIT measurements and which elements are assigned to the generation or application part. The generation part describes the experiment from entering the Intense XUV Beamline until the generation chamber where HHG is performed, and is discussed in Section 3.2. Various beam diagnostic instruments are applied along the whole beamline which are separately discussed in Section 3.3. The application part comprising the interferometer, diagnostics and application chamber is covered in Section 3.4. The central element is the double sided velocity imaging spectrometer (DVMIS) in the application chamber where the XUV and IR pulses are applied to investigate the interaction between atomic or molecular gases and the incident radiation. The Generation part of this original setup has been upgraded

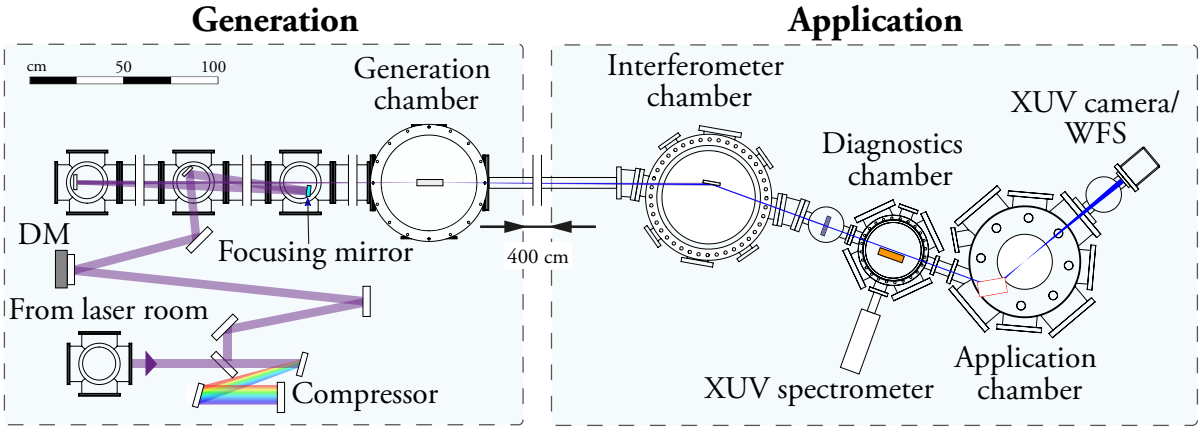

Figure 3.1: Intense XUV Beamline as it hase been used to perform the RABBIT scans. The pulses coming from the terawatt laser system generate XUV radiation in the generation part. These radiation is then characterized and applied in the application part. Figure adapted from [16].

during the time this master project was conducted. The crucial improvements are described in the results under Section 4.3.

3.1 The Terawatt Laser System

The Terawatt Laser System generates high energy pulses pulses with 400 mJ and low repetition rate. Figure 3.2 sketches the different parts of the setup. The laser is seeded with a Ti:Sapphire oscillator with high repitition rate in the MHz-range. A pulse picker then reduces the number of pulses to 10 Hz and guides the laser into a preamplifier. The preamplification increases the temporal contrast of the pulse which reduces spontaneous emission when passing the amplifiers after the stretcher. The first step of CPA (I: stretch, II: amplify, III: compress) is performed. Two optical gratings are adjusted parallel to each other under a certain angle of incidence, so that the pulse duration is stretched while the bandwidth remains. This is necessary to stay below the critical intensity that destroys the amplification medium. Different stages of amplification are then performed by flashing with frequency doubled Nd:Yag-pump lasers ($\lambda = 532\,\text{nm}$) into Ti:sapphire crystals. This optical pumping leads to a population inversion in the Ti-sapphire-material. The traversing pulse is amplified by the gain medium due to stimulated emission. After passing through a regenerative and a multi-pass amplifier, the spatial profile is shaped by a spatial filter. The beam is splitted in two parts of equal intensity. One part is guided to the

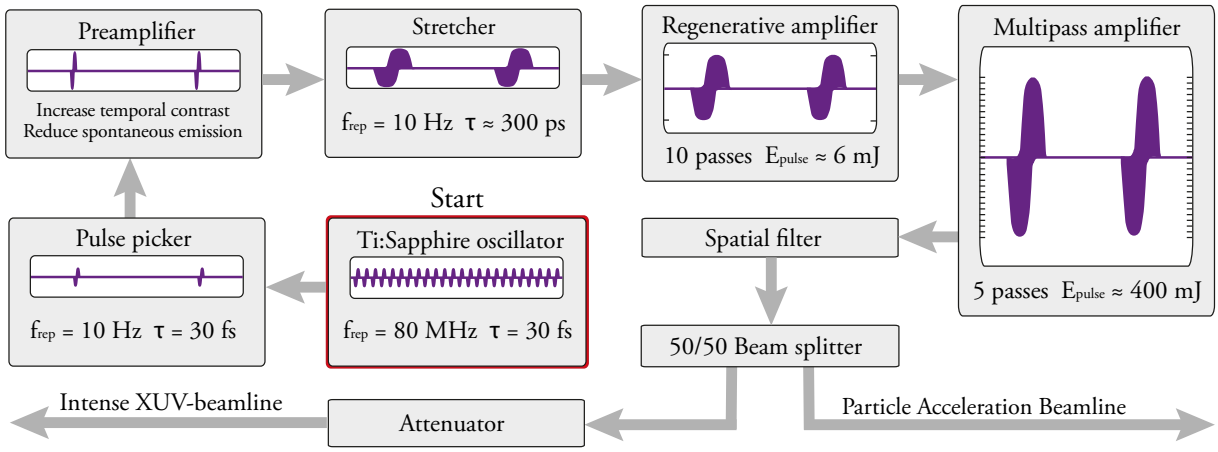

Figure 3.2: Schematic drawing of the the Terawatt Laser System. The pulse goes through several stages of amplification and beam treatment before leaving towards the experiment.

particle acceleration beamline, a different experiment which is not part of this thesis work. The other half ($\sim 200\,\text{mJ}$) is guided towards the Intense XUV beamline. This beam passes through an attenuator, consisting of a motorized $\lambda/2$-plate and a polarization dependent beamsplitter. The ratio of s- and p-polarization depends on the angle of the wave-plate and hence the ratio of transmitted to reflected light. The reflected s-polarized part is guided onto a beam blocker while the transmitted beam is forwarded to the experiment. This setup allows to attenuate the intensity of the beam reaching the Intense XUV Beamline. Mirrors, irises and camera alignment points are used to align the beam iteratively. The uncompressed pulse duration is in the range of several hundred picoseconds when leaving the laser room.

3.2 The Intense XUV Beamline: Generation part

The generation part of the Intense XUV Beamline generates XUV radiation via high harmonic generation using the pulses from the Terawatt Laser System. Figure 3.3 sketches the different parts and the beam path through the experiment. This section describes the setup as it has been used during the RABBIT experiments.

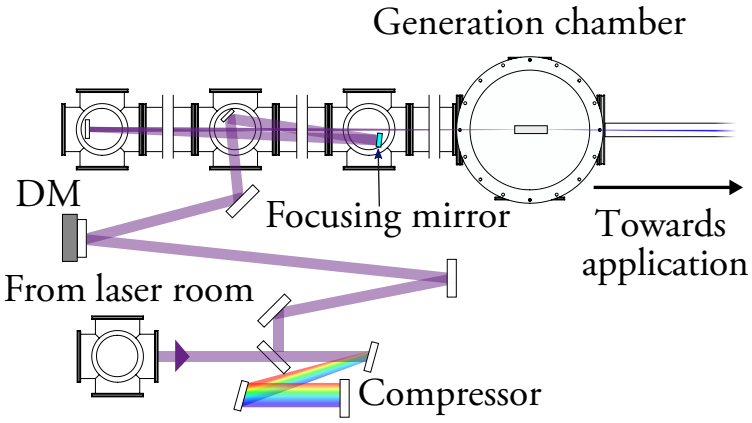

Figure 3.3: Topview of the HHG generation part at the Intense XUV beamline. The beam from the Terawatt Laser System is compressed, aberration corrected and focused on the generation gas argon. The generated high harmonic XUV radiation is then used in the application part of the setup. Figure adapted from [16].

The beam enters the setup from the vacuum transport tubes (Figure 3.3 to the left). The third step of CPA is performed by compressing the beam to the ultrashort pulse duration of $\tau \approx 35\,\mathrm{fs}$ using two parallel compressor gratings. A pulse energy of $\approx 50\,\mathrm{mJ}$ remains. The compressed beam is then guided on a deformable mirror (DM) (see next Section 3.2.1) for compensating wavefront aberrations and adjustment of the focus position. A flat wavefront assures good phase matching conditions for the HHG. Phase matching is necessary to avoid destructive interference of the higher harmonics leading to a loss in XUV stability and loss in yield. Furthermore, the relative intensity between different harmonics depends on the phase matching [20]. A mirror with a long focal range $f \approx 8.7\,\mathrm{m}$ focuses the beam onto the generation gas which is typically argon or neon. The focused beam is guided through a high vacuum ($p = 10^{-6} - 10^{-7}\,\mathrm{mbar}$) to prevent the strong field from generating an intensity reducing plasma in air and self-focusing. The long focus length is required to assure a large focal volume of high intensity $\sim 10^{14}\,\mathrm{W/cm^2}$ with a relatively great diameter. This creates a large interaction region within the tunneling regime and thus a high HHG yield. The gas source can be either a gas cell (of one or several cm length) or a gas jet as one compromise is between the stability of harmonic emission and the flux. The gas pressure is another parameter that strongly influences the phase matching conditions. The gas dispense is pulsed and triggered to match with the incoming laser pulse and still remain a high vacuum. However, the RABBIT scans analyzed in this thesis work had been performed with an argon gas jet. A typical energy range for high harmonics generated in argon gas at the Intense XUV Beamline is $E_{\mathrm{ph}} \approx 17 - 60\,\mathrm{eV}$ (11th - 39th harmonic). Section 3.4.2

contains two typical XUV spectra as they are measured with the spectrometer at the beamline. The total pulse energy of the XUV attosecond pulse train is $\approx 1\,\mu$J.

3.2.1 The Deformable mirror

The wavefront W(r,θ) of a beam is defined by the points at which the single waves of a deconstructed beam have the same phase. As previously mentioned, the optimal wavefront for HHG is flat to ensure best phase matching conditions and thus high XUV yield. The wavefront of a pulse coming from the Terawatt Laser System can be imagined as a crumpled piece of paper. There is various reasons for wave-front aberrations, such as deteriorated areas in the spatial filter, uneven pumping of the optical gain medium or degraded mirrors. An aberrated beam causes an uneven intensity distribution in the focus and the phase matching conditions are altered when generating harmonics. The DM is an element that compensates for these aberrations. Figure 3.4 is a schematic drawing of system. It consists of a membrane mirror with 32 piezoelectric actuators attached to the backside. These actuators shape the surface in a way that the reflected beam is aberration corrected. A signal from the wavefront sensor (see Section 3.3.2) located later in the beamline is required. An additional large actuator on the backside allows to change the curvature of the whole surface, imitating a focus mirror. This allows to move the focus of the IR by several meters.

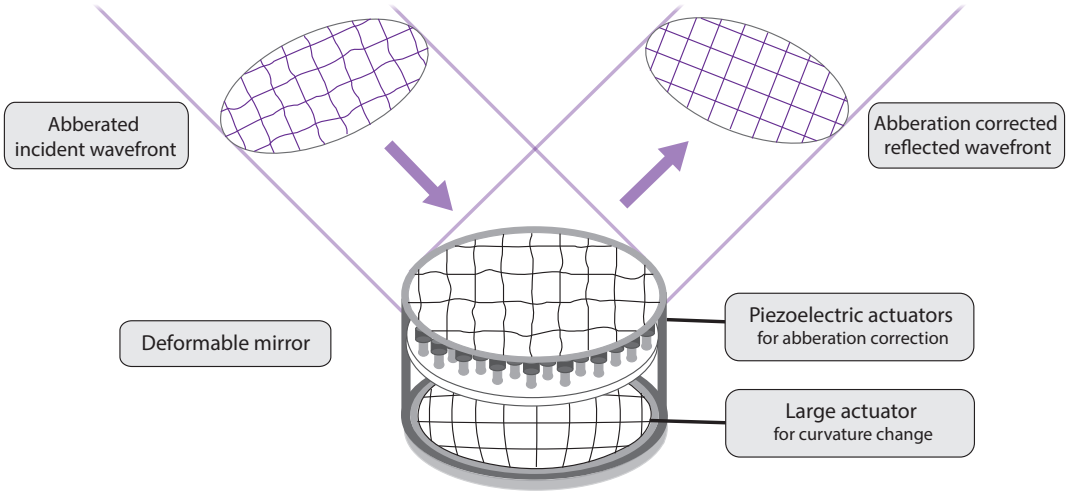

Figure 3.4: Schematic drawing of the deformable mirror, consisting of a surface with 32 piezoelectric actuators to shape the surface, as well as one larger actuator which changes the curvature of the mirror. This can be used to adjust the focus position in a range of several meter.

3.3 Beam Diagnostics

Beam diagnosing instruments are used to monitor properties of the laser such as pulse-duration, intensity or focus characteristics in order to improve and remain the conditions of the experiment. This section describes two non-trivial instruments which are deployed at the Intense XUV Beamline, the autocorrelator and the Wavefront sensor (WFS).

3.3.1 The Autocorrelator

The Autocorrelator is a tool to determine and monitor the pulse duration of the fundamental laser after compression. Figure 3.5 is a schematic drawing of the present setup. A mirror leak is taken as the input. The beam is splitted into two rays of equal intensity inside the device. One part is guided through an adjustable optical line slightly altering the propagation path with respect to the other ray to achieve the maximal overlap inside the $\chi^{(2)}$-nonlinear medium. This is the case when both rays have exactly the same propagation length.

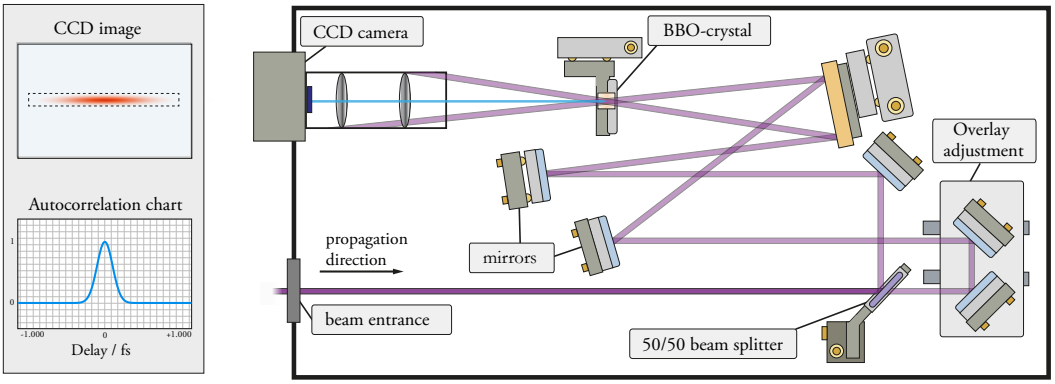

Figure 3.5: Sketch of the autocorrelator setup applying non-collinear SHG. The beam entering to the left is splitted into two rays of equal intensity. The rays are non-collinear overlaid inside a Barium borate BaB_2O_4 (BBO) crystal. The adjustment unit is set to create the maximal overlap between the pulses. The intensity of the SHG is visible on the Charge-coupled Device (CCD) camera. The pulse duration is extracted from the camera signal depending on the induced delay time.

The intensity peaks (with $f_{\text{rep}} = 10\,\text{Hz}$) arriving at the same time in the BBO crystal undergo a non-linear sum frequency generation resulting in SHG emission. Due to the non-collinear overlay the broadness of the SHG is determined by the pulse duration. The spatial intensity profile of the SHG, imaged by the CCD camera contains the temporal resolution of the IR pulses. The duration is determined by applying a conversion that depends on the original pulse shape and the specification of the autocorrelator. Changing the distance and relative angle between the compressor gratings minimizes the pulse duration. This is done on a daily basis. Typical values for the pulse duration measured at the Intense XUV Beamline are $\tau \approx 37 - 40\,\text{fs}$. A disadvantage of the presented technique is the averaging of the result over several laser shots due to the exposure time of the camera. Single shot measurements cannot be performed.

3.3.2 The Wavefront Sensor

The wavefront sensor is essential for feeding back signal to the DM software in order to correct for distortions. Such a sensor consists of a Hartmann mask, an opaque mask with a hole pattern or micro lens array, and a camera [21]. Figure 3.6 shows the schematic principle behind the WFS. Every hole in the pattern is acting like a lens, imaging the incident light as a dot on the camera sensor located in the focal plane. For a plane wavefront, this lens array will be imaged as a pattern of equidistant dots. This ideal case is setting the reference. A distorted wavefront will lead to a displacement of the focus from the reference position. Adding up the single displacements to a full image gives the complete wavefront image with all abberations.

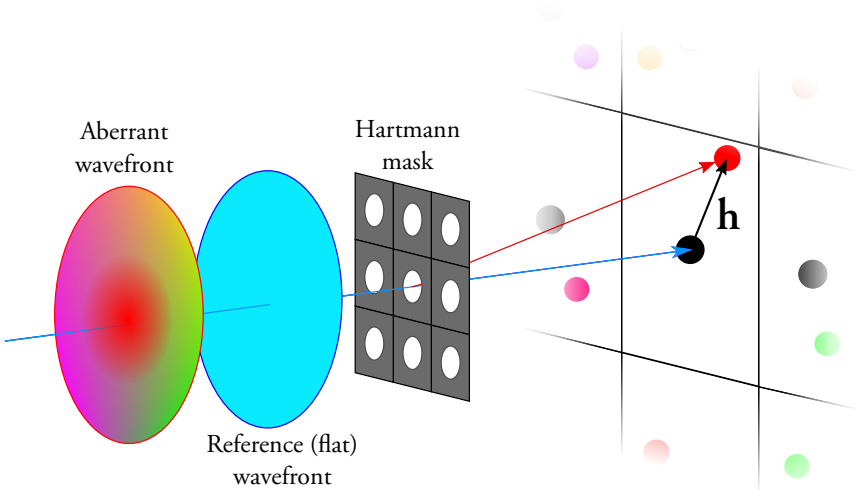

Figure 3.6: Wavefront sensor working principle. The raster represents the camera sensor. A flat wavefront is imaged straight behind the Hartmann mask on the sensor (black), while the aberrant wavefront image is displaced (red). Figure taken from [16].

The wavefront is monitored while changing the DM actuators. The signal is then decomposed into a sum of Zernike polynomials $Z_n^m(r,\theta)$

$$W(r,\theta) = \sum_{n,m} C_n^m Z_n^m(r,\theta) \quad , \tag{3.1}$$

with the Zernike coefficient C_n^m [22]. Zernicke polynomials give results in the interval $[-1,1]$. Every n-order Zernicke polynomial can be assigned to a certain type of aberration such as tilt, defocussing or astigmatism (see Figure 3.7). The angular frequency m defines the orientation of the distortion. The aberration assigned to the Zernike polynomial which has the biggest Zernike coefficient after reconstructing the beam wavefront predominates the distortion. By weighing the impact of the different coefficients C_n^m under variation of the DM membrane (toggling the piezoelectric actuators step-wise), a response function is created. The distorted incoming

wavefront is smoothed by applying this response function on the DM surface.

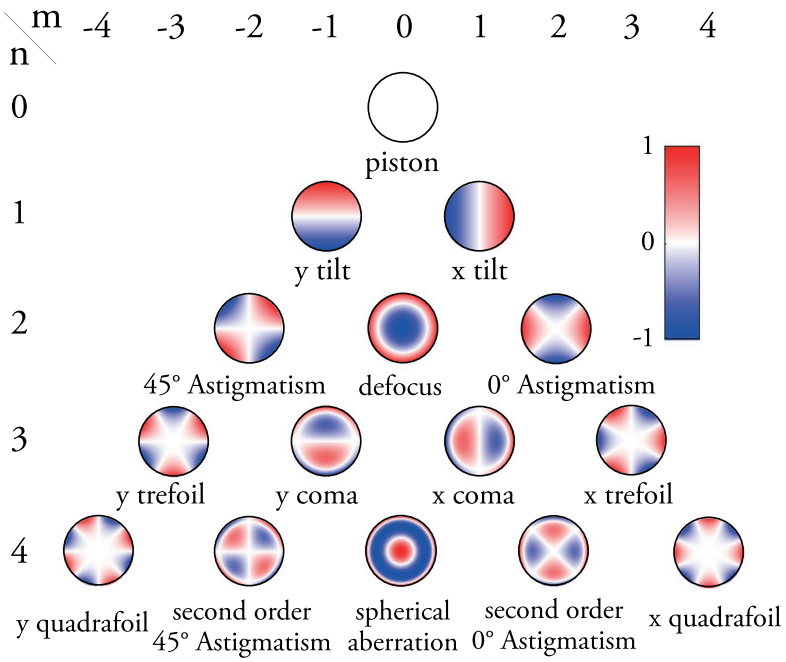

Figure 3.7: Zernike polynomials up to the $n = 4$ order of aberration. The common names are assigned to each aberration phenomenon. The angular frequency m is the repetition number of the alternating pattern and defines the orientation of distortion.

3.4 The Intense XUV Beamline: Application part

The application part comprises the interferometer chamber housing the XUV-IR interferometer (section 3.4.1), the diagnostics chamber and the application chamber. The central element inside the diagnostics chamber is a rotatable gold mirror. The incident beam can either be guided into the application chamber or reflected to the reference spectrometer or an alignment point.

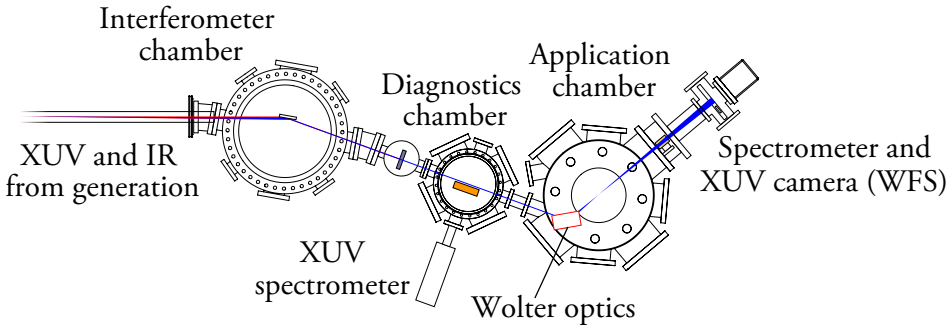

Figure 3.8: The application part of the Intense XUV Beamline. The XUV-IR beam is entering from the left and passes through interferometer and diagnostics chamber. The Wolter optics focus into the center of the application chamber where the target gas is released from a top-mounted Even-lavie valve. Figure adapted from [16].

The application chamber is housing the Wolter optics, focusing the beam in the middle of the chamber (section 3.4.3). Atomic or molecular gas is released in triggered bursts into the center from a topside located Even-Lavie valve [23]. The photoelectrons and ions generated in the region of interaction between gas and radiation are investigated with the Double Sided Velocity Map Imaging Spectrometer (DVMIS) (section 3.4.4). The back end consists of the XUV spectrometer and an Andor XUV camera that can be operated as a wavefront sensor by moving a Hartmann mask in front of the sensor. Five turbo-molecular pumps are keeping an ultra-high vacuum ($p \approx 10^{-8}$ mbar) in the chamber.

3.4.1 The Interferometer Chamber

The pulse from the generation part of the setup entering the interferometer chamber contains both fundamental IR as well as XUV radiation. Different setups can be implemented in the chamber, depending on the purpose of measurement (see Figure 3.9). The simplest installation consists of one single or two XUV mirrors (SiO_2 plate), reflecting the incoming beam to the application chamber but attenuating the IR light (Figure 3.9 I). The XUV Split-and-delay unit (Figure 3.9 II and Figure 3.10 *XUV split mirror assembly*) consists of two planar mirrors side-by-side to each other which can be translated independently [24]. The center of the XUV beam is aligned to meet the edge between the mirrors. Thus, moving just one mirror back will split the beam in two fractions, of which one gets delayed according to the extension of the optical path length (two times the distance between the two mirrors minus the angle projection). This setup allows to apply XUV-XUV probing assuming the IR is filtered out by an aluminium filter. Finally, the XUV-IR interferometer embraces all possibilities of pump-probing (Figure 3.9 III

and Figure 3.10). It combines all the features of the prior setups, to delay the IR and the XUV pulse with respect to each other and/or filtering out one of the components. The interferometer had been invented and implemented in the Intense XUV Beamline by H. Wikmark in 2019 [16]. The profound analysis of the delay scans generated by applying this XUV-IR interferometer for the first time is part of this thesis work.

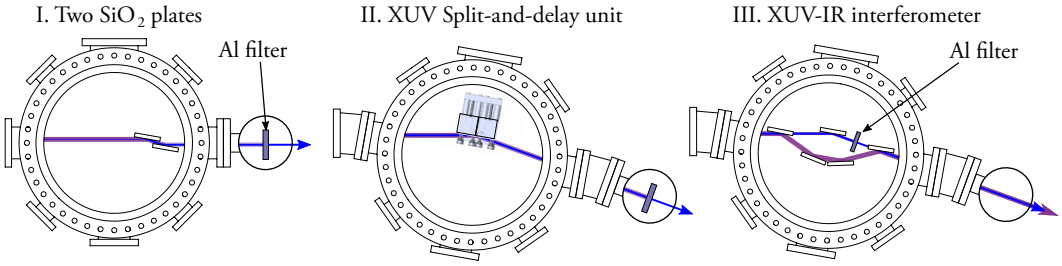

Figure 3.9: Different configurations of XUV-IR treatment which can be realized with the setup in the diagnostics chamber of the Intense XUV Beamline. Figure adapted from [16].

The working principle is based on the physical differences between the XUV and IR. The XUV has a smaller divergence and thus spreads less than the IR over the same propagation length. This is utilized to spatially separate them by a holey mirror, reflecting the outer ring containing only IR but letting pass the XUV through the middle. The two rays propagate along different arms through the interferometer. The remaining IR radiation in the XUV arm is filtered out after the XUV split-and-delay unit (XUV split mirror assembly). A delay line in the IR arm allows to extend the optical path length and thus the time delay of the light when both IR and XUV are merged at the second holey mirror. It is still possible to perform XUV-XUV probing with this setup if the IR light is filtered out [16].

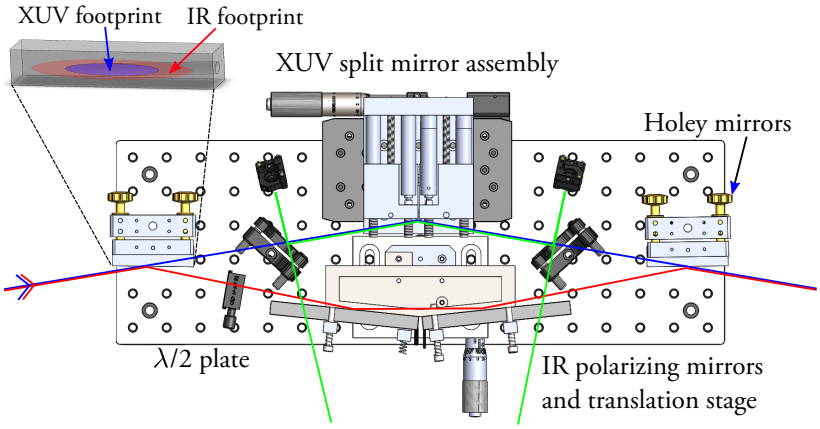

Figure 3.10: Drawing of the XUV-IR Interferometer. The beam from the generation entering to the left gets splitted into IR (red) and XUV (blue) using a holey mirror. Both beams propagate through separate paths which allows to induce a delay in the IR or split and delay the XUV. A second holey mirror merges the two beams. Drawing taken from [16].

3.4.2 The Diagnostics Chamber - XUV Spectrum

The interferometer chamber is followed by the diagnostics chamber which features a rotatable gold mirror as central element. The mirror can be arranged to either reflect the incoming beam towards an instrument attached to the diagnostics chamber or let the beam pass the following chamber without any interaction. One instrument is the spectrometer which had been used at the time of the RABBIT scans. To image the frequency components onto different positions of a sensor, the beam is getting dispersed by a toroidal grating. Calculating the pulse duration applying the RABBIT method requires the relative intensity of the interacting XUV spectrum. The measured intensity profile has to be corrected by the grating diffraction efficiency that is determined by the material and grating coefficient and usually handed by the manufacturer.

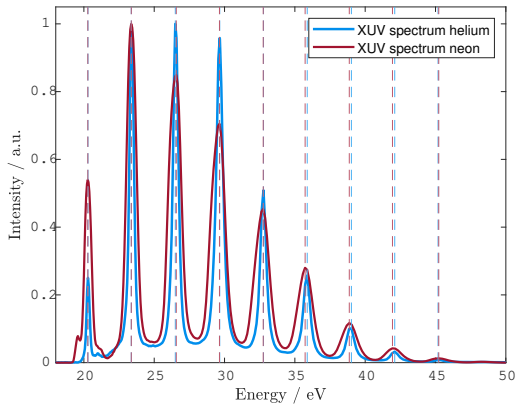

Figure 3.11: XUV spectrum generated in Argon, taken at the time of the RABBIT-scan in helium or neon. The spectrum is corrected for the grating efficiency.

Harmonic	Helium I / a.u.	Neon I/ a.u.
13	0.25	0.54
15	0.99	1.00
17	1.00	0.85
19	0.96	0.71
21	0.51	0.45
23	0.26	0.28
25	0.10	0.12
27	0.032	0.042
29	0.008	0.013
31	0.003	0.004

Figure 3.12: Relative intensity of the high harmonics, normalized to the integral of the strongest harmonic. The values represent the peak height to the left.

However, there are two spectrometers located around the application part. The second spectrometer at the back side of the application chamber was installed during the time of this thesis work. It is at the same position as the XUV camera. This has the advantage that the beam properties are the same for both measurement methods. It also enables to monitor the spectrum while measuring without the need to switch the gold mirror in the diagnostics chamber.

3.4.3 XUV focussing

The XUV-IR beam diverges after leaving the focus in the generation chamber. After passing through the interferometer and diagnostics chamber a refocusing is performed by Wolter-like optics [25] [26]. This configuration of two toroidal mirrors has a demagnificaiton of 35. Each of the mirrors is designed to suppress the chromatic aberrations induced by the other one. The focal length of $f = 170 \pm 1\,\mathrm{mm}$ is designed to have the highest intensity where the gas is released by the Even-Lavie valve, in the middle of the application chamber. Piezo-driven actuators and motors are attached to all five axes, the vertical and horizontal goniometer, the rotation stage

and the two translation stages (as depicted in Figure 3.13) for aligning the assembly. The alignment can either be done using the wavefront sensor on the other side of the application chamber or by optimizing the signal of the DVMIS.

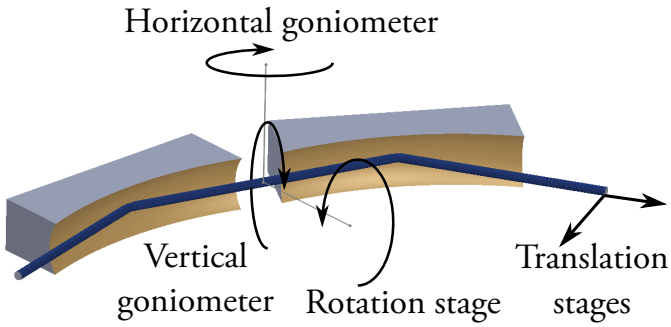

Figure 3.13: Wolter-like XUV-IR-focusing setup showing the five movable axes. Figure adapted from [27] .

3.4.4 Double-sided velocity imaging spectrometer (DVMIS)

As mentioned in section 2.4, a photoelectron spectrometer is used to determine the kinetic energy of the photoelectrons emitted due to XUV and IR ionization of the target gas. The novelty of the DVMIS setup is the possibility to not only record angle and energy resolved electron emission but also the angle-resolved kinetic energy of the ions and their mass-over-charge ratio in the operation mode of time-of-flight of charged fragments spectrometer. The DVMIS is a setup consisting of metal plates with holes (Figure 3.14). A voltage is applied to create an electric field pushing the ions towards the ion flight tube and the electrons towards the electron flight tube. The Micro-Channel Plate (MCP) amplifies the signal to be visualized on the phosphorus screen with sufficient intensity. Charges with low kinetic energy appear more to the center

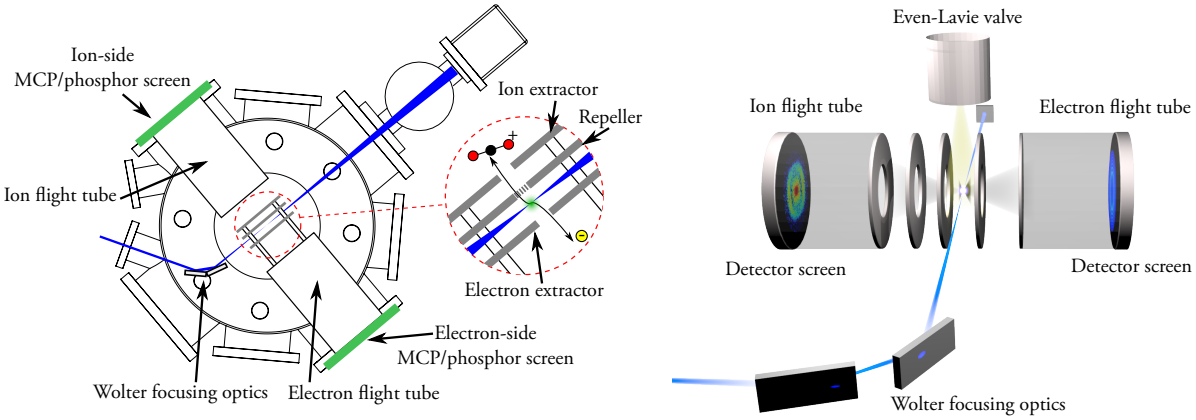

Figure 3.14: Detailed sketch of the application chamber with the laser coming from the left, passing through the Wolter optics to be focused in the center of the DVMIS. Behind that is the Andor XUV camera and the spectrometer. Figures taken from [16] and adapted from [28].

of the image. High kinetic energy charges drift further to the sides before hitting the screen and show up closer to the edges. The highest energy that can be imaged is defined by the

screen diameter and the adjusted voltage. Off-centering due to misalignment or not perfectly paralleled electrodes lowers the manipulation range. Figure 3.15 a) shows the resulting electron image captured with a camera imaging the screen. The harmonics and sidebands are arranged in rings around the center where the low kinetic electrons impact. The acquisition of these single images over a range of delay steps is the RABBIT-scan (Figure 3.15 b)). The polarization axis

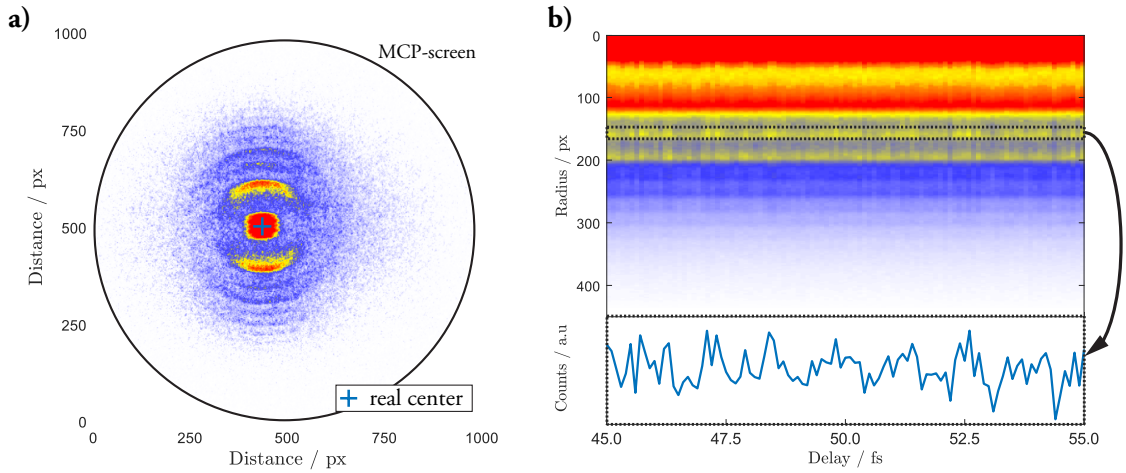

Figure 3.15: a) Raw single acquisition image without further correction. The black circle marks the round phosphor screen. The real center marks the place where the zero and low kinetic energy electrons impact the screen. The harmonics and sidebands are symmetrically arranged around this center. b) Angular integrated, re-centered and normalized image scanned over a delay range, using helium as the target gas. The line plot is the integrated signal of the first sideband.

of the laser field (vertically polarized) is along the vertical line through the *real center*. The bottom curve of Figure 3.15 b) shows the sideband signal as an integration over a certain radius as a function of delay. An oscillation can be seen to some extent, but a phase reconstruction is rather difficult and not of high quality. This is why a thorough data analysis and statistics are needed for the analysis.

4 Analysis, results and discussion

The previous chapters introduced the principle and requirements on how to apply the RABBIT technique. However, the extraction of information from the measurement is not trivial. This chapter is about the signal analysis and evaluation of delay scans of HHG created in argon on two different atomic target gases. Filtering and statistical tools are applied to receive the sideband phases. Section 4.1 is about the investigation of the helium measurement, starting with the pre-processing of the raw measurement and continuing with the determination of the phase and calculation of the relative harmonic emission time delay τ_{atto}. The determination of τ_{atto} and the reconstruction of the temporal properties of the attosecond pulses the target gas neon are described in Section 4.2.2. However, the analysis is not exactly the same due to different signal rates and scan lengths. Resampling is introduced as a means to improve single image quality of long scans. This enables the study of an angle-resolved features. Finally, Section 4.3 is about the redesign of the generation part of the Intense XUV Beamline that has been conducted to improve the stability of the system. The actual setup of the experiment and its advantages to the previous design are pointed out.

4.1 Helium analysis

Helium is a noble gas with an ionization potential of $I_p = 24.58\,\text{eV}$. Noble gases have in general a high ionization energy due to their electron configuration. Given our XUV-spectrum, this leads only to single electron ionization which is crucial to understanding the dynamics as this is the simplest system. The ionization of the gas atoms is imaged by the DVMIS for both ions and electrons. One single image acquires 100 laser repetitions before going to the next delay step. A common scan length is in the range of several ten femtoseconds with a resolution of 0.1 fs leading to a data set of several hundred images. A reference XUV only picture without target gas and a background image is taken before and after each scan. The helium scan analyzed in this section is a sum of four scans between 45 and 55 fs. In this work we only consider the electron side to observe the ionization properties.

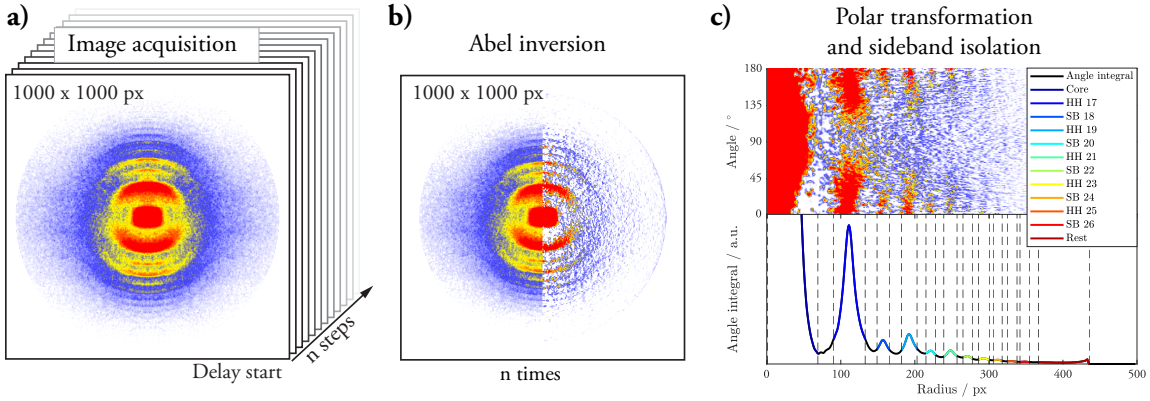

Figure 4.1: a) An image series of the MCP is acquired over a range of n delay steps. It is elliptical corrected and re-centered. The drawn picture shows a scan with helium as target gas. b) The Abel inversion optimizes the contrast and appearance of the structures in the raw measurement (left sphere) to more distinct lines (right sphere) and is individually performed on every single image. c) The inverted data set transformed into a polar coordinate system. The radius range of each harmonic/sideband is based on the broadness of peaks in this angle integral.

The data acquisition relies on the camera imaging of the phosphorous screen behind the MCP. Due to imperfections of the spectrometer, the ring-shaped structure of the raw data images can be slightly distorted and off-centered. Hence, the first step of correction is performed by re-centering the image and apply an elliptical correction. Figure 4.1 a) shows the elliptical corrected image for one delay step. The structure of the sidebands is smeared and not distinct. The reason for this lies in the principle of measurement. Electrons with a single kinetic energy end up on a sphere in momentum space. After passing through the flight tube, they hit on a two-dimensional screen. The initial three-dimensional distribution smears the circle on screen. An Abel inversion is performed targeting the image back on a two-dimensional cut through the three-dimensional distribution. The applied iterative method is written by M.J. Vrakking [29]. The direct comparison can be seen in Figure 4.1 b). The left half sphere is the image before and the right half sphere after the Abel inversion.

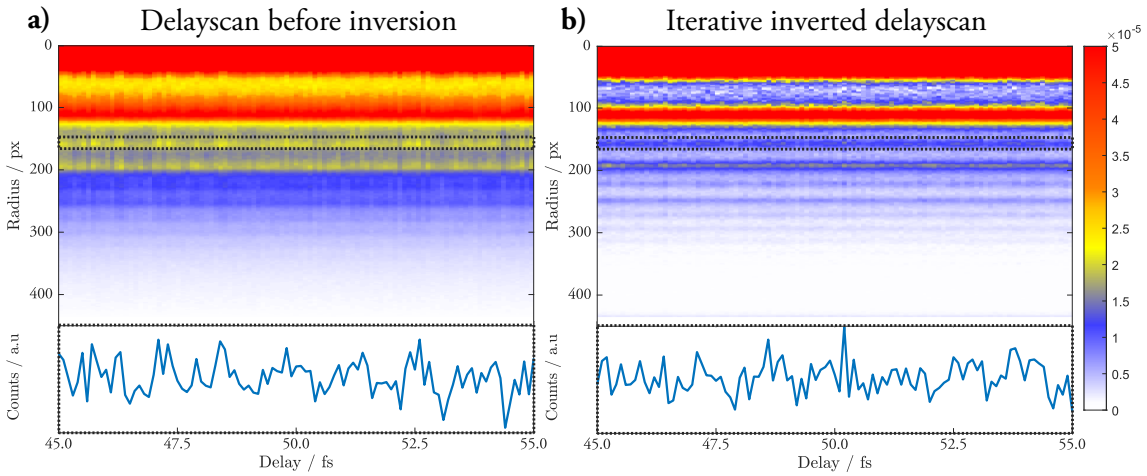

Figure 4.2: Radial distribution of the delay scan in helium before a) and after b) an iterative image-by-image inversion. The regions of harmonics/sidebands become more distinct due to the inversion and the contrast improves. The line to the bottom is the radial integration over the box in the image and shows sideband 18.

The image improvement due to inversion is judged by the contrast value. We define the contrast line by line for every radius r as:

$$C_{\mathrm{Img}}(r) = \frac{I_{\max}(r) - I_{\min}(r)}{I_{\mathrm{mean}}(r)} \quad . \tag{4.1}$$

The average over all radii $\bar{C}_{\mathrm{Img}}$ is giving the global contrast factor of the image. For the non-inverted data this value it $C_{\text{non-inverted}} = 0.194$ while the inverted data set has a contrast value of $C_{\text{inverted}} = 0.453$, more than twice the value before. This proves that the inversion enhances the information properties of the image considerably. The inversion assumes a symmetry axis which is set along the fundamental field polarization (vertical line through the center of image 4.1 a)). As a consequence of this, the image after inversion is left-right symmetric. In order to isolate the sidebands and harmonics arranged in circles around the center with different diameter, the Cartesian plot is transformed into a polar coordinate system (Figure 4.1 c) top). An integration over all angles as a sum of all delay steps creates a profile that shows a very distinct peak for each band (Figure 4.1 c) bottom). The radius range assigning the sidebands is based on this graph. The energy of the first harmonic q ionizing the electrons to be visible in the kinetic energy spectrum must be larger than the ionization potential of the target gas $\hbar\omega_{\mathrm{q}} > I_{\mathrm{p}}(\text{target})$. For helium this is calculated to $q_0 = \lceil I_{\mathrm{p}}/\hbar\omega_0 \rceil = 17$. A sideband only occurs in-between two harmonics. Hence, the next radius must be assigned to sideband $(q_0{+}1)$, followed by the harmonic $(q_0 + 2)$ and so on. This is done until the signal intensity vanishes. Figure 4.2 is a comparison of the full non inverted and inverted delay scan, showing all harmonics and sidebands depending on the time delay. The integration over the sideband radius for every single delay step returns the isolated sideband signal. Filtering is now applied on the data in order to remove noise and assure a good fit quality. To avoid a huge DC-component in Fourier space, the mean value is subtracted from all data points before Fourier transformation. An oscillation

is now visible as peak in the frequency spectrum (Figure 4.3 a)). This peak is then filtered out by multiplying the spectrum with an explicitly broad normalized Gaussian function, centered around the peak. The broadness of the filter allows the frequency to still vary between different sidebands. This is important since a too narrow filter function can induce oscillations to the signal which might be not there. That is a particular problem when the oscillation is in the order of the noise in Fourier-space.

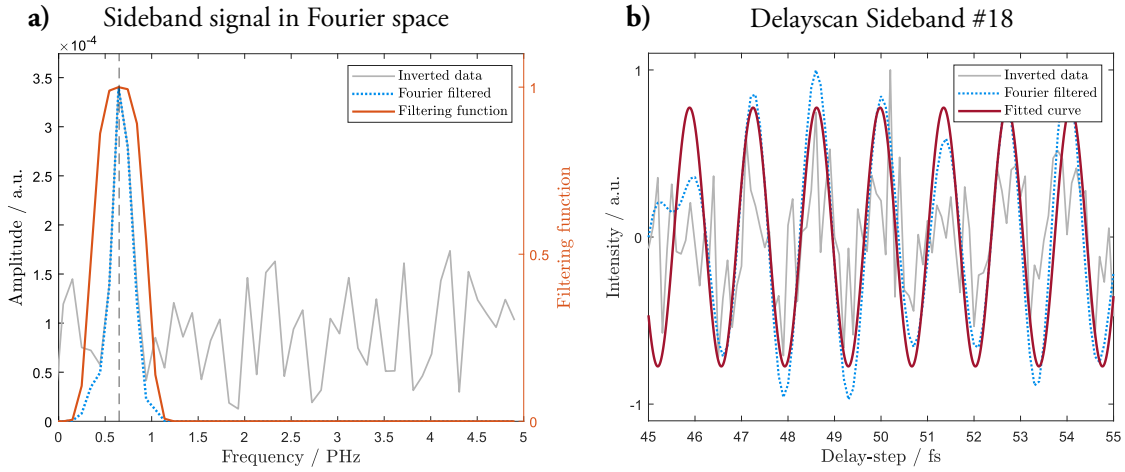

Figure 4.3: a) The sideband signal, corrected for the bias, and transferred into Fourier space (grey). A Gaussian filter function (orange) applied on the data returns the filtered signal (blue). b) Baseline corrected delayscan of isolated sideband 18 (grey), re-transformed delay scan after filtering (blue) and cosine fit function applied on the filtered data (red) to extract the phase.

The filtered data is re-transformed into the temporal domain, and a fit is performed. In accordance to Equation (2.19) from the theory, the fit satisfies a cosine function of the shape

$$f(x) = A \cdot \cos(\omega x - \varphi) \quad , \tag{4.2}$$

with the arbitrary amplitude A, the frequency ω and the phase shift φ. There is no correction for a shift in y-direction since any DC-components are taken away by the Fourier filtering. A first cosine fit is performed on all sidebands and harmonics, leaving all fitting parameters unlocked. The average frequency for the harmonics and sidebands between the 17^{th} and 23^{rd} order excluding clear outliers is determined to be

$$\omega = (4.6 \pm 0.1)\ 10^{15}\,\text{rad/s}\ . \tag{4.3}$$

Ideally, this frequency is equal to two times the frequency of the fundamental laser $\omega \approx 2\omega_0$, since one HHG burst is emitted every half laser cycle. However, the fundamental laser frequency is broad and the phase extraction has an error. By dividing this value by two, the wavelength of the fundamental laser can be calculated to $\lambda_0 = 819 \pm 18\,\text{nm}$. ω is now locked for the following phase extraction because a variation of the frequency during the fitting process affects the phase value. It would not be correct then to compare the phase shift between two different sidebands. The fit is then applied another time on the filtered signal, but with the frequency locked to the

determined value ω. The phases are extracted as listed in Table 4.1. Figure 4.4 displays the high harmonics and sidebands b) before- and after filtering as well as the fit result (red). The bands with order $q = 24$ and higher are not further considered because the fit quality was insufficient due to high noise.

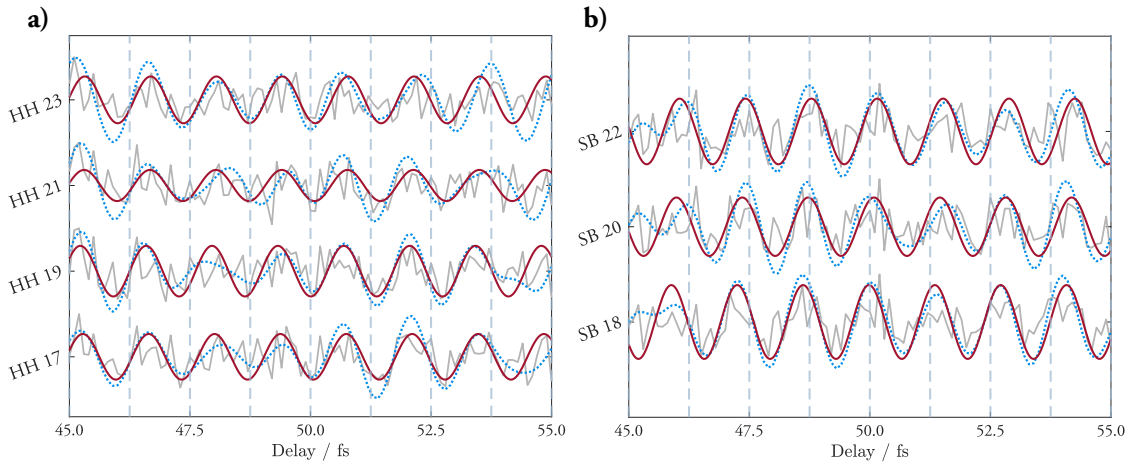

Figure 4.4: All high harmonic (left) and sideband oscillations (right) extracted from the helium target gas measurement. The baseline corrected signal (grey) is Fourier filtered (blue dashed) and fitted (red). The higher order signals are less intense and of worse quality. A remarkable feature is the π phase difference between sidebands and harmonics. This can be also utilized to distinguish one from another.

Without the presence of sidebands, high harmonics do not oscillate. However, the sideband excitation requires photons from the harmonic which then are not present there anymore. This is the reason why harmonics indeed oscillate due to depletion, but phase inverted with respect to the sidebands. A reconstruction of the temporal domain of the attosecond pulse based on the obtained phases would be possible but at this point not very reasonable. Only three the phases out of ten harmonics visible in the XUV spectrum could be determined. An interpolation based on three points is vague and the reconstruction would draw a false picture. The relative harmonic

Table 4.1: Extracted phases for the high harmonics and sidebands in Helium. τ_{atto} is calculated from the sideband phases.

Harmonic	**Phase/ rad**	**Sideband**	**Phase/ rad**	τ_{atto}/as
17	7.22 ± 0.13	18	3.72 ± 0.09	809
19	6.98 ± 0.13	20	4.20 ± 0.14	913
21	7.34 ± 0.26	22	4.50 ± 0.11	978
23	7.40 ± 0.18			

emission time can be derived for the visible sidebands. Referring to Equation (2.21), τ_{atto} is derived from the sideband phase, neglecting the small atomic contribution τ_{atomic}. The phase of the sideband oscillation is equal the phase difference between two consecutive harmonics. The harmonic emission time delay τ_{atto} of the subsequent harmonics is directly determined [18]:

$$\varphi_{\text{SB}}(\omega_{q+1}) = \varphi(\omega_{q+2}) - \varphi(\omega_q) + \varphi^{\text{atomic}}(\omega_{q+2}) - \varphi^{\text{atomic}}(\omega_q) \approx 2\omega_0 \tau_{\text{atto}}(\omega_{q+1}) \tag{4.4}$$

The phases of the sidebands 18, 20 and 22 from Table 4.1 are applied to calculate the emission time τ_{atto}. The RABBIT-technique can only derive the relative phase differences between two harmonics, but not an absolute phase value. The emission time difference between the harmonics is the difference between two sidebands: $\tau_{20} = \tau_{\text{atto (q = 20)}} - \tau_{\text{atto (q = 18)}} = 104\,\text{as}$, respectively $\tau_{22} = 65\,\text{as}$. We see that the emission time difference is in the order of magnitude of $\sim 100\,\text{as}$. However, the number of values is not sufficiently high. This is motivation for a deeper investigation on the neon data set where more sidebands can be observed.

Angle-resolved analysis of helium

As pointed out in the experimental approach, the advantage of the DVMIS in comparison to ordinary photoelectron spectrometers is the possibility to do angle-resolved measurements. By skipping the angular integration but still performing the radial integration over the sideband/ harmonics, one obtains the angle-resolved delay scan of a sideband. Figure 4.5 contains the angular resolved image of harmonic 17 and sideband 18. The angle-dependent count rate to the left hints on artefacts which are in the delay scan image. Here, harmonic and sideband electrons are clearly emitted in the same direction along the same axis 0/180 °. There might be a feature in the sideband at 90 °, but the signal is weak and this bump can also be caused by noise.

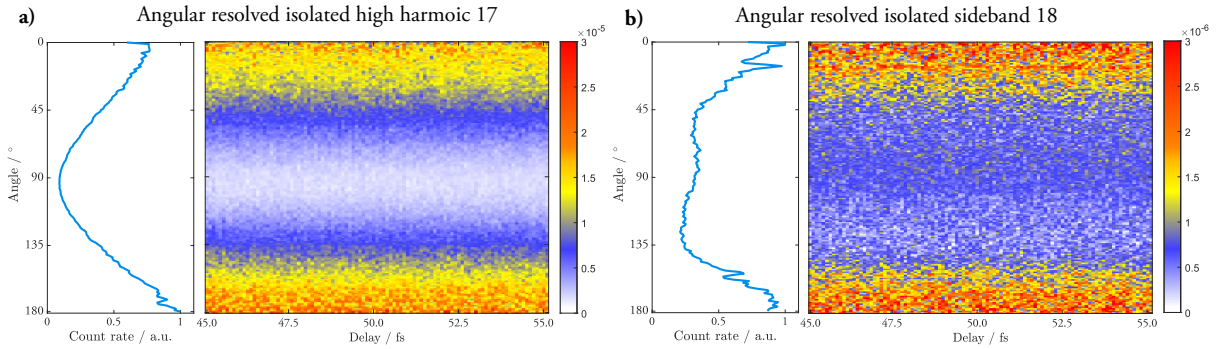

Figure 4.5: Angular resolved isolation of the harmonic $q = 17$ Figure a) and sideband $q = 18$ Figure b). The left curve beside the image represents the integration over all delay steps and represents the count rate per angle.

Harmonic 17 and sideband 18 have already the most intense signal. Therefore, the even higher orders do not give a better resolution than what is visible in Figure 4.5 since they are weaker. It is not possible to state a clear conclusion based on these images.

4.2 Neon analysis

Neon has an ionization potential of $I_p = 21.56\,\text{eV}$ which is around three eV lower than helium. The RABBIT-scan with neon as target gas consists of a long delay scan from 40 to 100 fs with 0.1 fs delay-step (helium: 45 to 55 fs). Therefore, the single image signal intensity is lower and less statistics is available compared to the four overlaid scans in helium. The first part of the analysis is performed analogue to the previous section. Additional tools are then applied to improve the quality of the result. The single images are re-centered and corrected for elliptical distortions. The iterative Abel inversion is performed (Figure 4.8 a)) before the Cartesian image is transformed into a polar coordinate system 4.8 b)). It becomes visible in the polar transformation (Figure 4.6 b)) that the emission of sidebands from a neon target gas is shifted by 90 ° with respect to the harmonics. This angle dependency will be investigated later in this chapter. The spherical integration over all delay steps enables to assign the radius to the order of each harmonic and sideband 4.6 c)). The first visible harmonic is defined via the ionization potential to $q = 15$. Furthermore, harmonic number 15 shows an abnormality of three visible peaks, here called 15-1, 15-2 and 15-3. A first analysis shows that only 15-2 is clearly oscillating. Hence, this radius range will be taken for the investigation on harmonic 15.

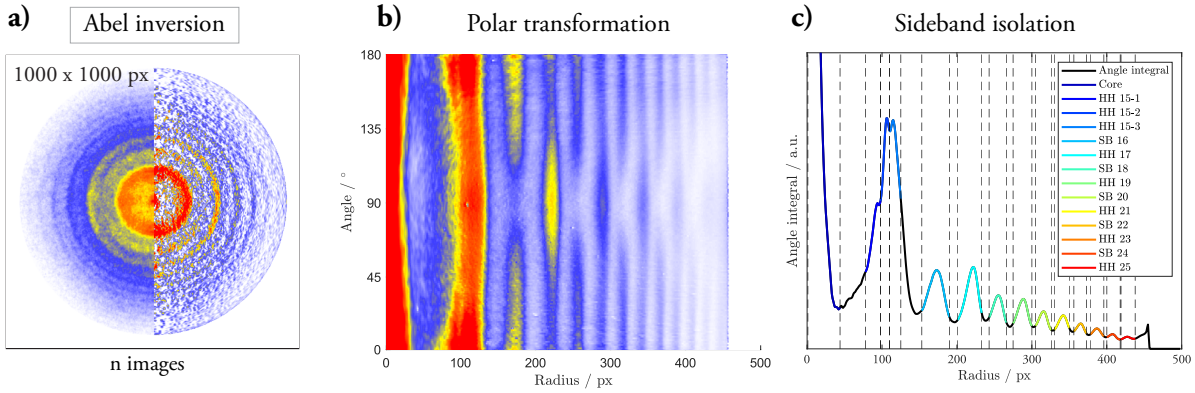

Figure 4.6: a) The iterative Abel inversion of the spherical corrected image is performed for all single steps to receive distinct sideband areas. b) The spherical single images are transferred into a polar coordinate system for further analysis. The image here shows the sum over all delay steps to point out the angular features. c) Integration over angle and delay-steps to assign harmonic- and sideband ranges.

Figure 4.7 compares the complete delay scan before and after inversion. The contrast factor of the non-inverted image, calculated using Equation (4.1) is $C_{\text{non-inverted}} = 0.158$ which improves to the the value $C_{\text{inverted}} = 0.826$ after inversion. The single line obtained by integration over sideband 18 clearly shows an oscillation. At this point, this oscillation is quite noisy and cannot be directly used for phase extraction without undergoing signal treatment.

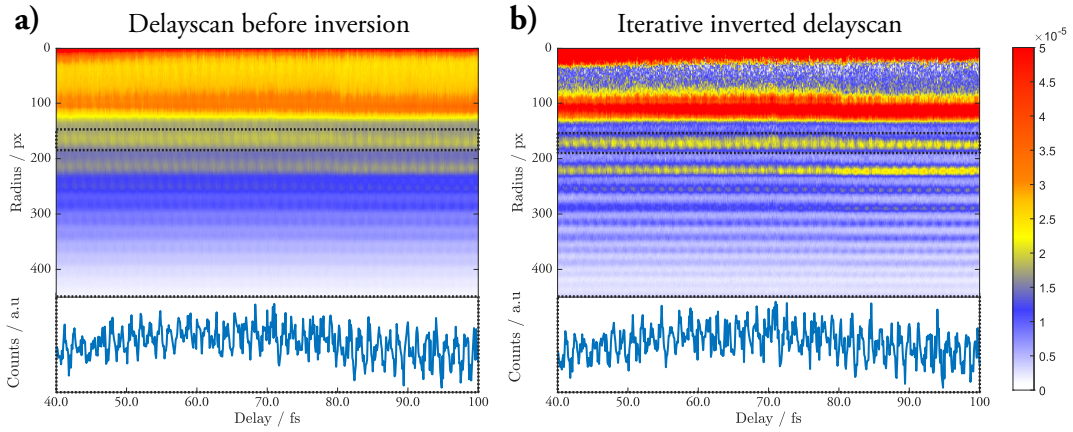

Figure 4.7: a) Angular integrated delay scan using neon as a target gas before a) and after inversion. The line to the bottom is the radial integration over the box in the upper image and represents sideband 18.

The harmonics and sidebands are transformed into Fourier space to perform a filtering analogue to the helium analysis. Figure 4.8 a) contains the inverted and baseline corrected data set (grey) and the normalized Gaussian filtering function (orange) centered around the clear oscillation frequency peak. The filtered data set (blue) is free of higher and lower frequency components. A cosine fit with unlocked parameters is performed on the re-transformed data (like Figure 4.8 b)) on all harmonics and sidebands. The oscillation frequency is determined to

$$\omega = (4.631 \pm 0.012)\ 10^{15}\,\mathrm{rad/s}\ . \tag{4.5}$$

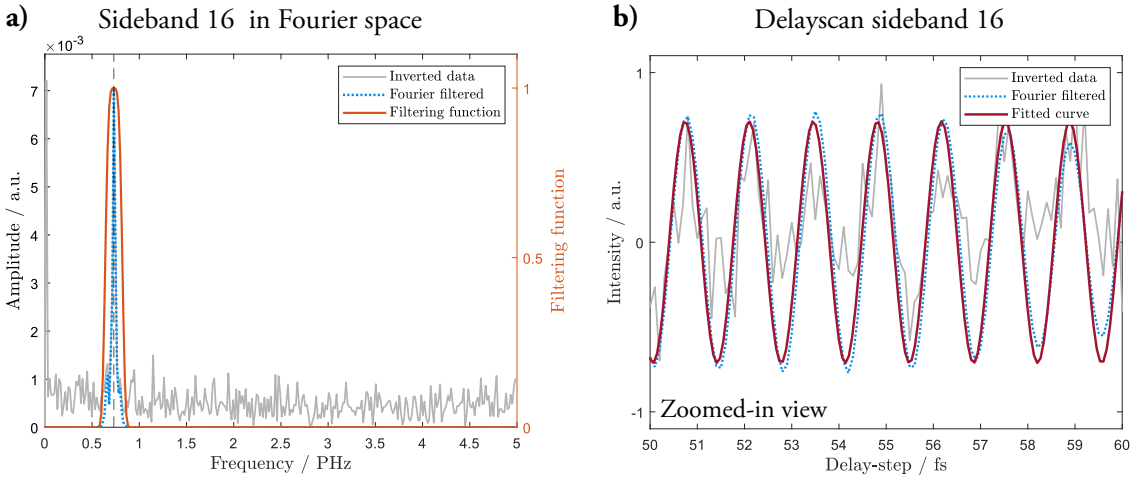

Figure 4.8: a) Fourier space including the baseline corrected angular integration (grey), a normalized Supergaussian filter function (orange) and the filtered curve (blue line). b) Raw image sum (grey) and re-transformation of the filtered data set (blue). A cosine fit is performed on the filtered data (red line).

A second fit is performed locking the frequency to the average value from Equation (4.5). The result gives the phase differences for sidebands and harmonics as they are written in Table 4.2. Figure 4.9 contains all harmonics and sidebands before and after filtering as well as the

fit functions. The signal to noise ratio (SNR) is better than in helium allowing to extract the phase of even higher sidebands (up to the 24th order).

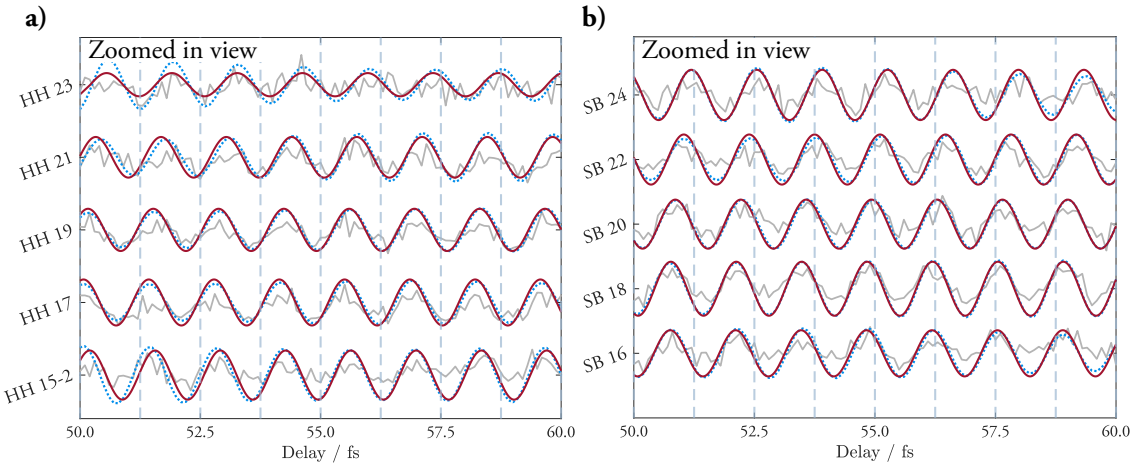

Figure 4.9: Harmonics a) and sidebands b) that could be acquired by the analysis of the RABBIT scan using the target gas neon. Zoomed in view of the scan, originally spreading from 40 to 100 fs. Harmonics and sidebands are phase inverted here as well.

The emission time delay τ_{atto} is calculated from the sideband phases, applying the approximation of a small atomic contribution as done before for the helium analysis:

$$\varphi_{\text{SB}}(\omega_{q+1}) \approx 2\omega_0 \tau_{\text{atto}}(\omega_{q+1}) \quad . \tag{4.4}$$

The resulting times can be found in the right column of Table 4.2 and are plotted in Figure 4.10.

Table 4.2: Phase-shifts for the bands extracted by fitting to the Fourier filtered data.

Harmonic No.	**Phase**	**Sideband No.**	**Phase**	τ_{atto}/as
15	6.292 ± 0.007	16	2.569 ± 0.026	555
17	5.687 ± 0.004	18	2.625 ± 0.003	567
19	6.121 ± 0.004	20	3.055 ± 0.003	660
21	6.864 ± 0.004	22	3.868 ± 0.003	835
23	7.91 ± 0.13	24	4.598 ± 0.004	993

By performing a linear fit on the emission times in Figure 4.10, we receive the relative emission time delay:

$$\Delta\tau_{\text{atto}} = 114 \pm 61\,\text{as} \quad . \tag{4.6}$$

This relative harmonic emission time delay had been emasured for harmonics between the 11^{th} and 25^{th} order, generated and detected in argon gas by Y. Mairesse et al. [18]. A very similar setup with a slightly higher intensity but the same fundamental wavelength had been used. One crucial difference is the detection of the harmonics generated in argon by argon as target gas instead of neon. The results were also validated with theoretical predictions. The relative emission delay had been determined to $\Delta\tau_{\text{atto}}^{\text{exp}} = 106 \pm 8\,\text{as}$ for the experiment and $\Delta\tau_{\text{atto}}^{\text{th}} =$

81 ± 3 as based on theory. This is well in accordance to the result that had been calculated based on the measurement in our setup and supports the correctness of this analysis.

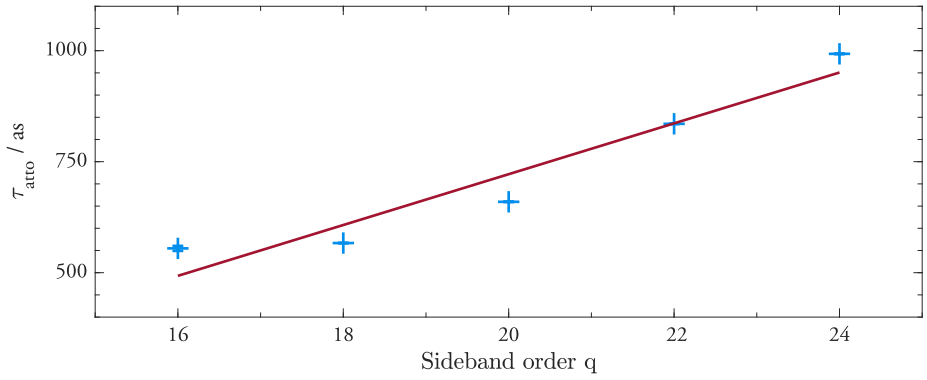

Figure 4.10: Emission time delays for all sidebands (blue markers). A linear fit is performed (red line). The slope is the relative emission time delay.

4.2.1 Reconstruction of attosecond pulse trains

To reconstruct the temporal domain of the attosecond pulse train, the sideband phase differences and relative intensities from the spectrum (Table 3.12) are required. Equation (2.18) from the theory is extended to include all sideband phases. However, the reconstruction will be incomplete as the values from Table 4.2 do not contain the phase information of all contributing harmonics in the spectrum. The 13^{th} harmonic is not imaged by the photoelectrons due to the higher ionization potential of the target gas. Furthermore, the sidebands for harmonics above $q = 25$ could not be obtained because of the noisy signal. Fitting a linear function, analog to Figure 4.10 but to the phase values, and interpolating the phases of the remaining sidebands overcomes this problematic. The reconstruction is performed up to the 30^{th} sideband since this covers the highest harmonic of the order $q = 31$ visible in the XUV spectrum.

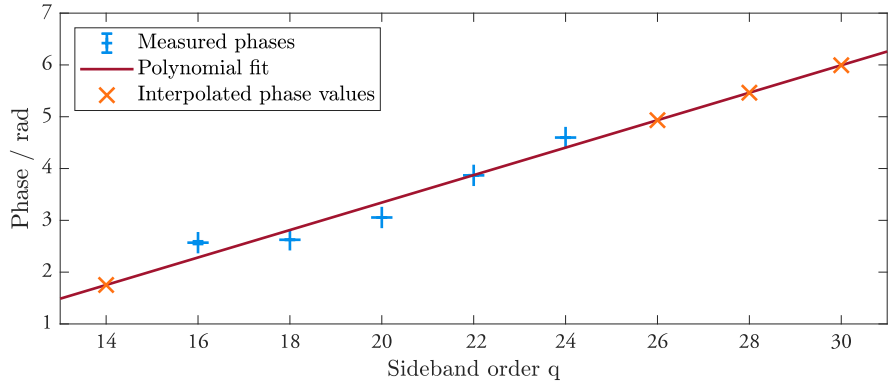

Figure 4.11: The sideband phases (blue markers) are fitted with a linear function (red line) to interpolate phase values for the sidebands which could not be determined with the delay scan (orange markers).

Figure 4.12 contains the temporal reconstruction of the attosecond pulses based on the sideband phases from Table 4.2 and including the interpolated phase values. The pulse duration

(FWHM) of the temporal domain using only the extracted phases of sidebands 16-24 is derived to:

$$\tau = 313\,\text{as}\,. \tag{4.7}$$

Considering Equation (2.11), the real pulse duration is likely to be smaller than this value when all harmonics are taken into account and if the phase does not contribute destructively. Especially the 13^{th} harmonic which could not be measured but interpolated is of high relative intensity and thus largely affecting the interference process. The dashed blue line in Figure 4.12 is the reconstruction including the interpolated phases. The shortest pulse is the Fourier limited pulse which is composed of the same number of harmonics and intensities, but without any phase difference between consecutive harmonics.

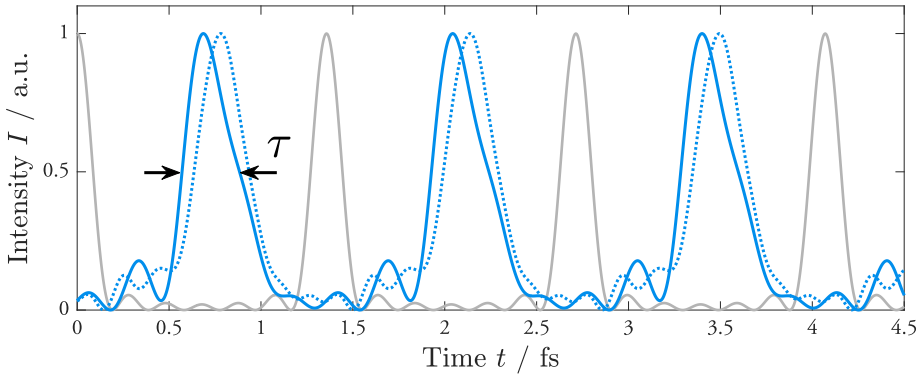

Figure 4.12: Temporal reconstruction of the attosecond pulses based on the relative intensity of the XUV spectrum and the phases obtained by the RABBIT method (blue). The dashed blue line is the reconstruction including the interpolated phases. The pulse duration τ is given by the FWHM of the peak. The grey line represents the theoretical Fourier-limited pulse including the same harmonics.

Including the interpolated phases, the duration reduces to $\tau = 299\,\text{as}$. Both results are in a reasonable order of magnitude since the duration of the Fourier limited pulse spanning from harmonic order $q = 13$ to 25 is determined to $\tau = 173\,\text{as}$. The phase is also adding a group delay, leading to a shift of the peaks in the figure with respect to the Fourier-limited curve. Since the initial phase of the sideband is arbitrary, this shift is arbitrary.

4.2.2 Energy calibration

An energy calibration of the radius scale of the DVMIS is conducted. The frequency ω_0 extracted from the Fourier-filtered data fit (Equation (4.5)) is used to determine the energy of the present harmonics and sidebands. This energy is plotted over the radius of every sideband in the angle integrated plot. The trajectory of a charged particle in the electric field of the flight tube follows an acceleration due to Coulomb force. Thus, the Energy of the particles hitting the DVMIS screen is related to the radius squared:

$$E_{\text{kin}} \propto r^2 \quad . \tag{4.8}$$

A quadratic fit is performed to the set of points (see Figure 4.13 left). The intersection with the ordinate is by definition the ionization potential I_{p} and locked. The fit function is described by

$$E(r) = a(r)^2 + I_{\text{p}} \quad , \tag{4.9}$$

with the calibration coefficient a and the radius x in pixel. This method uses the assumption that all harmonics originate from the same IR frequency.

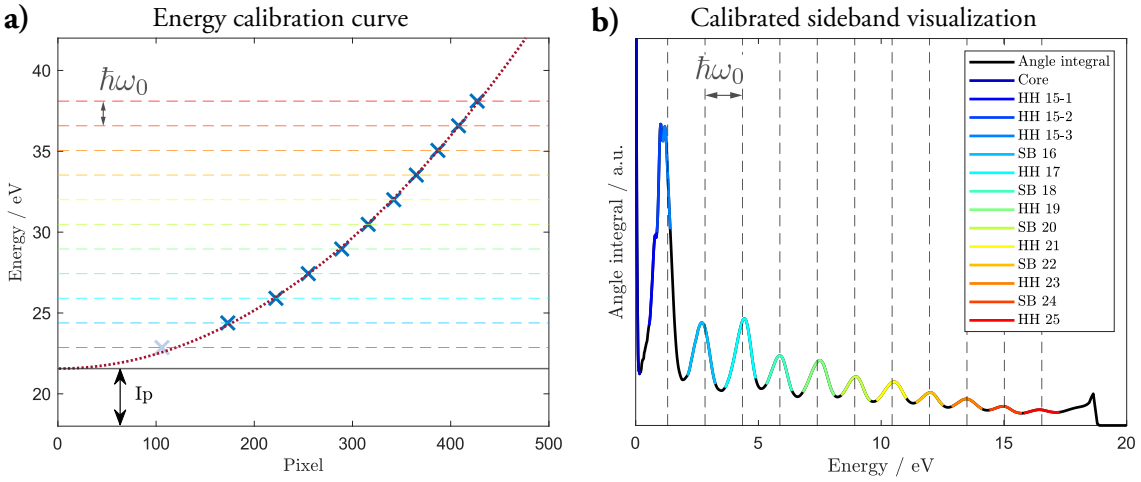

Figure 4.13: a) Energy calibration curve assigning an energy value to each pixel. The horizontal dashed lines represent the energy of the harmonic and are equidistant with a difference $\Delta E_{(\text{q+1})\text{-q}} = \hbar\omega_0$. b) sideband visualization applying the energy calibration on the data. The vertical dashed lines mark here the harmonic energies.

The ionization potential for neon is given with $I_{\text{p}} = 21.56\,\text{eV}$. Harmonic 15-2 is considered as an outlier as the value is systematically shifted towards lower energies (redshifted).

4.2.3 Data resampling

A long single image scan is not optimal for the analysis since the single image signal is relatively weak and largely affected by noise. A method to overcome this obstacle is a resampling of the data on a shorter interval giving better single image statistics. From the phase acquisition of the non-resampled scan, the oscillation frequency ω of the sidebands is known. The resampling is performed by expressing the time of the delay scan in multiples of the oscillation period. All images lying in a certain oscillation phase interval are then summed up to one single image. Thus, the data has been resampled from initially 600 delay steps to an interval of 27 steps before the inversion is performed. Particularly, the quality of the iterative inversion is expected to

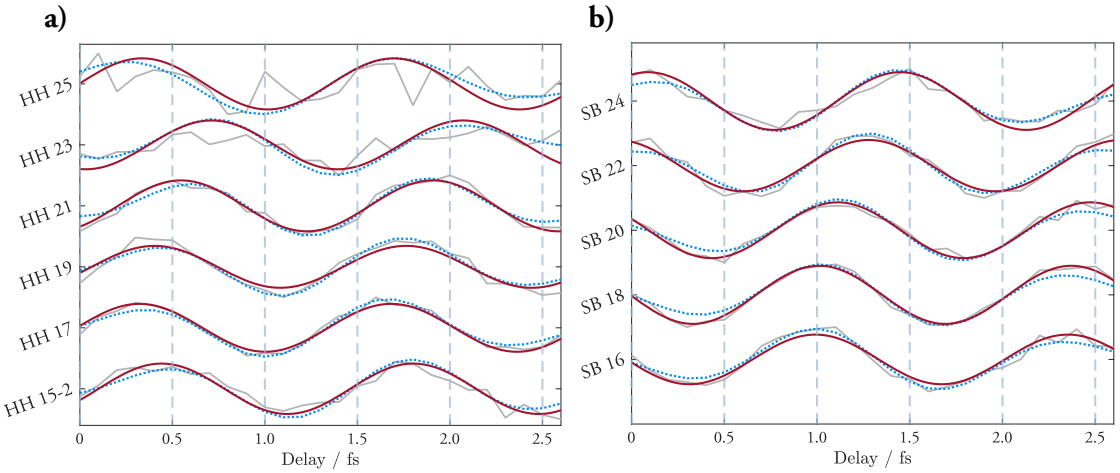

Figure 4.14: a) Harmonic and b) Sideband extraction for the resampled data set. The original data (grey) is Fourier filtered (blue) before a cosine function is fitted (red).

improve significantly from that. However, this is not necessarily to the advantage of the phase determination since shorter data scans provide a lower fit accuracy. As before, the average frequency of all harmonics and sidebands is locked when performing the phase fit. The determined frequency is:

$$\omega = (4.62 \pm 0.13)\ 10^{15}\,\mathrm{rad/s}\ . \tag{4.10}$$

This is in good agreement with the result on the non resampled data in Equation (4.5). Figure 4.14 contains the resampled fit results for both sidebands and harmonics with locked frequency ω. The resulting phases (Table 4.3) are compared to the non-resampled data (Table 4.2) in Figure 4.15. The initial phase is arbitrary, hence the relative phase differences of consecutive sideband must be compared. The relative emission time delay is derived from the slope of the red line in Figure 4.15. This leads to a value of

$$\Delta\tau_{\mathrm{atto}} = 118 \pm 59\,\mathrm{as}\ \ , \tag{4.11}$$

and is in accordance to the result for the non resampled data set. However, the benefit of the resampling is more visible in the features that can be seen in the single delay step images. Figure

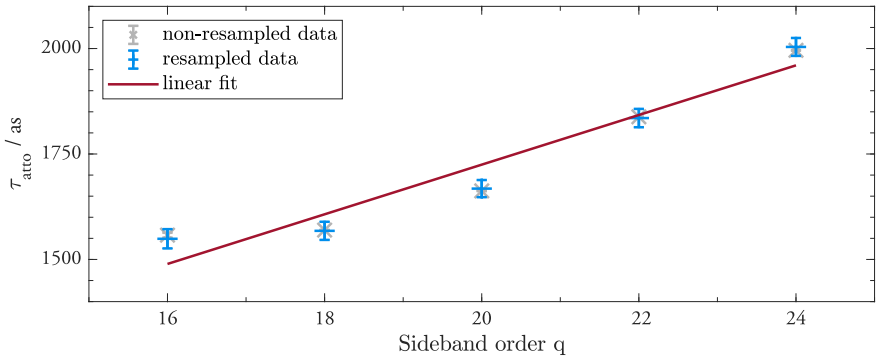

Figure 4.15: Resampled data (blue markers) over sideband order. A linear fit is performed (red line). The grey crosses represent the non resampled phase values, added with an offset to the mean value of the resampled data set. The markers are close to each other, which underlines that the phase extraction on the resampled data is of the same quality.

Table 4.3: Phases for the harmonics and sidebands from the analysis of the resampled data. Since the initial phase is arbitrary, the absolute values cannot be compared to the non resampled phases, but their relative differences.

Harmonic No.	**Phase**	**Sideband No.**	**Phase**	$\tau_{\mathbf{atto}}$/as
15	4.63 ± 0.09	16	7.17 ± 0.11	1549
17	4.08 ± 0.10	18	7.26 ± 0.10	1568
19	4.45 ± 0.12	20	7.72 ± 0.09	1668
21	5.11 ± 0.10	22	8.50 ± 0.10	1835
23	5.88 ± 0.15	24	9.28 ± 0.10	2004
25	4.14 ± 0.16			

4.16 is a comparison between the angle integral of conventional- and resampled data set. An improvement is clearly less noise in the resampled image. The triple peak shape of harmonic 15 (15-1, 15-2 and 15-3) is now considerably more distinct. Particularly the 15-3 peak which is not visible in the normal data gets a clear structure in the resampled image. This preservation of features in the single step image is of major interest for the angle-resolved analysis.

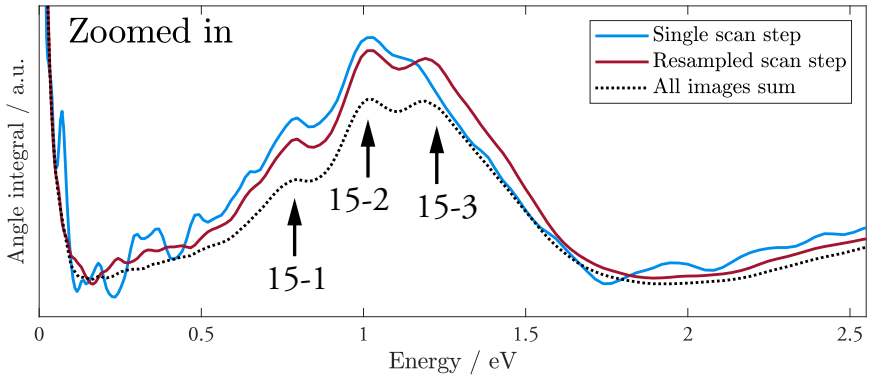

Figure 4.16: Calibrated angle integrated curves of single step image, resampled single step image and the image sum over the full scan. The noise of the resampled image is clearly less. This is important to be able to recognize features that are small in comparison to the signal fluctuations.

4.2.4 Angle-resolved analysis

The angle-resolved analysis is of major interest since this holds the potential to discover anomalies in the electron emission like angle dependency of the oscillations of the triple peak in harmonic 15. The improvement of angle dependent phase resolution of electron emission due to resampling is investigated on the showcase of sideband 16. The full scan is Fourier filtered and fitted with the cosine function. Figure 4.17 shows the angle-resolved image of sideband 18 before, and after filtering. A fit is performed with the frequency locked at $\omega = 4.631 \cdot 10^{15}$ rad/s.

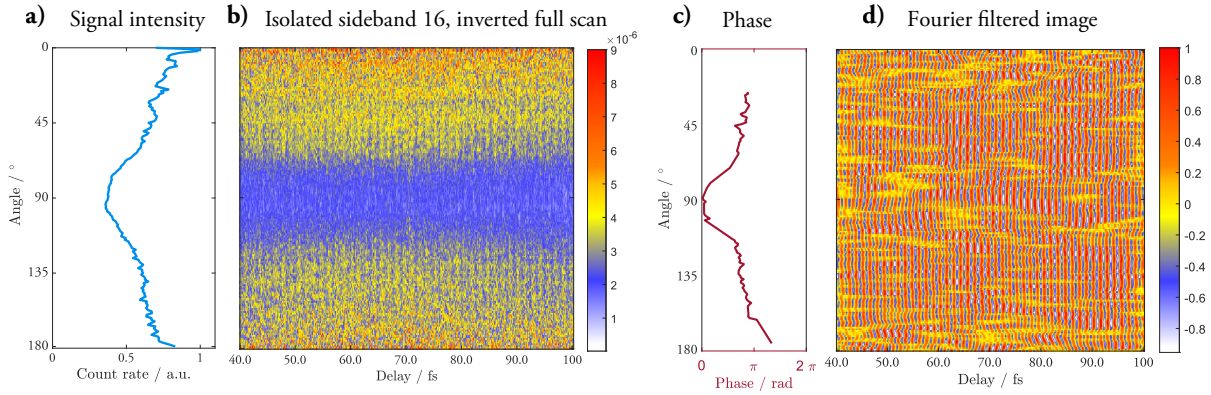

Figure 4.17: Angle resolved properties of sideband 16. The signal intensity hints to an oscillation induced by the Fourier filtering due to low SNR. b) Isolated sideband with angle dependency. The full scan is shown. c) Line-by-line phase extraction performing a cosine fit on the Fourier filtered full-scan in image d).

The phases are only depicted in the phase plot if the fit is of sufficient quality which means exceeding a correlation coefficient $r > 0.7$. The resampled data set (Figure 4.18) is undergoing the same analysis procedure as the full scan. The angular resolved phase can be visualized more precisely and detailed in comparison to the conventional analysis and more fits reach the quality requirement.

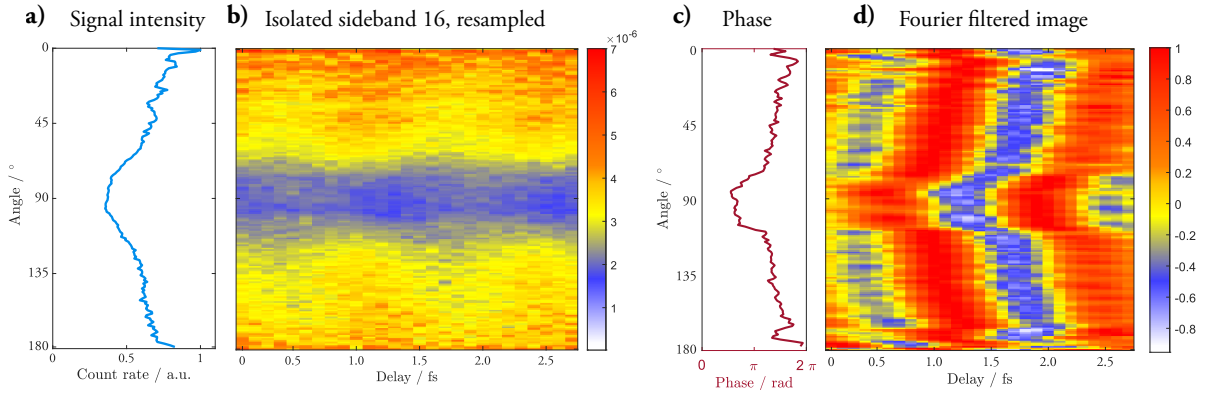

Figure 4.18: a) Signal intensity of sideband 16 along the sphere. b) Isolated sideband for the resampled data set. Figure c) contains the phase information which had been extracted from the cosine fit on the Fourier filtered data rows in image d).

At the same time, it is important to keep the signal intensity in mind, since the Fourier filtering can induce oscillations if the signal is too noisy. However, the intensity is sufficiently high over all

angles for this sideband. The angle-resolved analysis has clearly improved in comparison to the non resampled image. In this angle-resolved analysis of the sideband it becomes clearly visible that the electron emission at 90° degree is out of phase in comparison to 0°. The transition is fading depending on the angle until there is a step-like jump close to the vertical center. The interpretation of these features is up to the outlook.

4.3 Re-design of the generation part

There is a change of the laser properties over the time frame of a day due to rising temperature or realignment in between measurements. Hence, a higher stability of the setup is desirable. One crucial change on the Intense XUV Beamline during the time of this master project had been the setup of a new vacuum chamber for the generation part. Self-focusing and intensity losses in air are reasons to enter a vacuum even before focusing, as well as less dust accumulation on optics. The key elements (compressor, DM, focusing optics) remained. The novelty is in the more sophisticated arrangement of the beam path and standardized alignment procedures. The inaccessibility of the mechanics under vacuum requires motorization of all components. Vacuum compatible stages and mirror alignment motors in combination with a camera monitored alignment points were implemented. The transport tubes are directly connected to the compressor

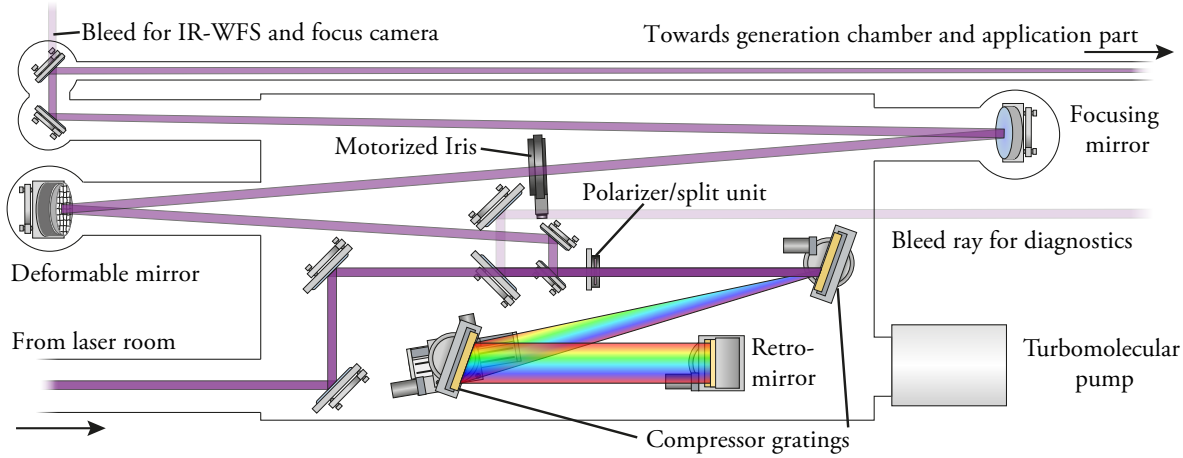

Figure 4.19: Drawing of the new generation chamber. The laser entering from the left bottom first propagates through the compressor. The polarizer/split unit allow to take out a part of the beam for beam diagnostics and other experiments. The leak through the last mirror is used for wavefront analysis (DM Input).

chamber and share the same vacuum. Turbo molecular pumps (TMP) are used to preserve a high vacuum of $p \approx 6 \cdot 10^{-6}$ mbar in this part of the beamline. The generation chamber (not in the image) has two more TMPs attached to perform a differential pumping with respect to the compressor chamber. Thus, the gas released in the generation chamber cannot migrate to the compressor part. A valve is separating the chambers physically when no beam is in use. New gratings on high precision motorized mounts are arranged to compress the pulse down to $\tau \approx 40$ fs. The ability to alter the focus by the DM by a motorized iris and the attenuator in the

laser room is applied to optimize the IR properties in the generation gas. The split unit consists of a $\lambda/2$-waveplate and polarization-dependent mirrors operating like a beamsplitter. The angle of the waveplate determines the intensity of the bleed ray exiting to the right hand side. This beam is used for pulse length analysis (Autocorrelator, D-scan) and other experiments. The leak through the mirror before the gas cell is used to determine the wavefront aberration and correction with the DM. Furthermore a camera at the approximate focal distance monitors the spatial profile of the focus. The optimized alignment routine and additional monitoring possibilities, together with the motorization of parts which were operated manually before have proven to ensure a better reproducibility of the day to day beam properties. The application of a high vacuum and the use of new optical components improved the stability and intensity of the setup.

5 Conclusion and outlook

This thesis work is about the theoretical and experimental requirements on the generation of attosecond pulses as a light source for the investigation of charge dynamics. The second chapter states the theory behind attosecond pulse generation using high harmonic generation explained by the Three-Step Model. A method to retrieve information about the time domain of such attosecond pulses is the Reconstruction of Attosecond Beating By Interference of Two-photon Transition (RABBIT). The experimental approach is presented in chapter 3 with the setup of the Terawatt Laser system and all sections of the Intense XUV Beamline in the LLC. High harmonics created in argon gas are characterized using two different target gases, helium and neon. Each RABBIT scan consists of a set of DVMIS images over the delay between XUV and IR radiation. An Abel inversion is performed on every single image to replicate the real two-dimensional image from the three-dimensional projection on the detector and improve the contrast of the scan. After isolating the sidebands and harmonics according to their photon energy, Fourier filtering is applied and a cosine fit performed to obtain the phase signal of the oscillation. The harmonic emission time delay τ_{atto} is calculated for the present harmonics. Furthermore, the temporal domain of the attosecond pulses is extracted based on the phases obtained from a long delay scan with neon as target gas. This reconstruction of the pulse returns a pulse duration of $\tau = 313\,\text{as}$, based on the measured phases. An interpolation is applied to obtain the attosecond pulse duration with all contributing harmonics of the spectrum. Including the interpolated phases, the calculated pulse duration reduces to $\tau = 299\,\text{as}$. An energy calibration of the radius of the DVMIS is performed.

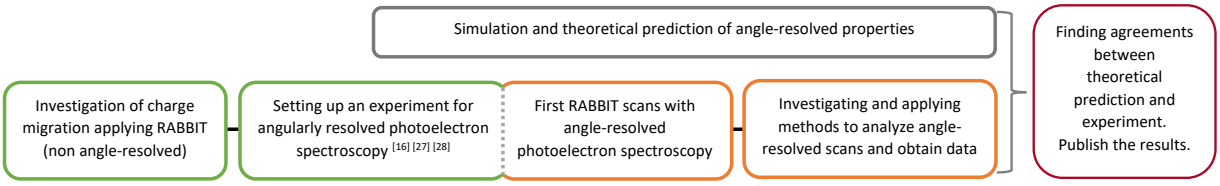

Figure 5.1: Assessment of the contribution of this thesis work to the ongoing research. Green: status of experiment and research before this thesis work. Orange: Contribution of this thesis work. Grey: parallel ongoing research on theory related to the experiment. Red: Future steps, outlook.

Figure 5.1 is an assessment of the contribution of this thesis to the research progress on charge dynamic investigation. The setting up of the experiment had been done before this thesis work. The first angle resolved RABBIT delay scans at the Intense XUV-Beamline were briefly investigated by Hampus Wikmark in his PhD thesis [16]. This work and is about the analysis and analysis improvement of these measurements. Resampling of long scans is stated as a method to considerably improve the angle-resolved measurement by increasing the single step image statistics while preserving the phase extraction quality. The angle-resolved analysis is of major interest and had been investigated in the kHz-laser-system at the Lund Laser Center [12]. A first investigation exposes that helium sideband photoelectrons are emitted in the same

orientation (0/360 and 180°) as the fundamental laser while sideband emission in neon takes mostly place orthogonal to the field (90/270 °). At this point, the experimental results have to be compared with theory in order to be able to publish the findings in the frame of a scientific article. Finally, the upgrade of the generation part of the experiment is presented as an improvement of the current setup which had been implemented during the time of this thesis work. The standardization and automation of alignment procedures as well as the application of a high vacuum over the hole generation part lead to an improvement of stability and intensity.

Outlook

An application of the introduced angle-resolved analysis procedure on all sidebands and a detailed comparison with both theoretical simulations and the experimental results from the Lund kHz Beamline is reasonable to verify the findings. Furthermore, the upgrade of the generation part promises higher stability and better signal in future scans. The qualitative improvement had been already proven but the positive influence on the RABBIT scan is up to being quantified at this time. Conducting longer scans with different atoms or small molecules for detection under application of XUV-IR or XUV-XUV pump-probing has not been done yet. This holds potential for discoveries which contribute to the understanding of molecular dynamics.

6 Acknowledgements

First, I want to thank all my colleagues at the atomic physics department. I have been there for quite some time now, so I thank those who left during my work, Jan Lahl, Hampus Wikmark and Hugo Dacasa, and those who started, Maria Hoflund. A special thank is addressed to those who have accompanied me the whole time. Thank you Jasper Peschel for the co-supervision, for your patience to explain all the things I did not understand after the meetings, the great socializing and the never ending proofreading. Thank you Per Johnsson for all what comes when being the main supervisor. You are a never ending source of ideas to tackle theoretical and practical problems. Thank you Cord Arnold for having paved my way to the atomic physics department. We never know what would have happened if I had decided for your degree project. Thank you Anne L'Huillier for guiding us through science, in good and in bad times. I am sorry if I forgot to mention somebody here. It is not personal, but I have to be brief. Its finally not a PhD thesis.

I would like to thank my family and parents for their support. I had all the great opportunities, doing my Abitur after the secondary school, learning to play instruments, study at a university, travel a lot and pursuing my Master's in Sweden. I know you worked hard for making this possible. The years of financial support are finally coming to an end in the age of 27.

Bibliography

[1] T. H. Maiman. "Stimulated optical radiation in ruby".
In: *nature* 187.4736 (1960), pp. 493–494.

[2] P. A. Franken et al. "Generation of Optical Harmonics".
In: *Phys. Rev. Lett.* 7 (4 Aug. 1961), pp. 118–119. DOI: 10.1103/PhysRevLett.7.118.

[3] L. Keldysh et al. "Ionization in the field of a strong electromagnetic wave".
In: *Sov. Phys. JETP* 20.5 (1965), pp. 1307–1314.

[4] D. Strickland and G. Mourou. "Compression of amplified chirped optical pulses".
In: *Optics Communications* 56.3 (1985), pp. 219–221. ISSN: 0030-4018.
DOI: 10.1016/0030-4018(85)90120-8.

[5] M. Lewenstein et al. "Theory of high-harmonic generation by low-frequency laser fields."
In: *Physical Review A (Atomic, Molecular, and Optical Physics)* 49.3 (1994), pp. 2117–2132.

[6] S. Svanberg et al. "Lund high-power laser facility–systems and first results".
In: *Physica Scripta* 49.2 (1994), p. 187.

[7] P. Antoine, A. L'Huillier, and M. Lewenstein.
"Attosecond Pulse Trains Using High–Order Harmonics".
In: *Phys. Rev. Lett.* 77 (7 Aug. 1996), pp. 1234–1237. DOI: 10.1103/PhysRevLett.77.1234.

[8] P. M. Paul et al.
"Observation of a Train of Attosecond Pulses from High Harmonic Generation".
In: *Science* 292.5522 (2001), pp. 1689–1692. ISSN: 0036-8075. DOI: 10.1126/science.1059413.

[9] T. Gaumnitz et al. "Streaking of 43-attosecond soft-X-ray pulses generated by a passively CEP-stable mid-infrared driver". In: *Optics express* 25.22 (2017), pp. 27506–27518.

[10] P. Hockett. "Angle-resolved RABBITT: theory and numerics".
In: *Journal of Physics B: Atomic, Molecular and Optical Physics* 50.15 (2017), p. 154002.

[11] C. Cirelli et al. "Anisotropic photoemission time delays close to a Fano resonance".
In: *Nature communications* 9.1 (2018), pp. 1–9.

[12] D. Busto et al.
"Fano's Propensity Rule in Angle-Resolved Attosecond Pump-Probe Photoionization".
In: *Phys. Rev. Lett.* 123 (13 Sept. 2019). DOI: 10.1103/PhysRevLett.123.133201.

[13] K. J. Schafer et al. "Above threshold ionization beyond the high harmonic cutoff".
In: *Phys. Rev. Lett.* 70 (11 Mar. 1993), pp. 1599–1602. DOI: 10.1103/PhysRevLett.70.1599.

[14] S. Augst et al. "Laser ionization of noble gases by Coulomb-barrier suppression".
In: *J. Opt. Soc. Am. B* 8.4 (Apr. 1991), pp. 858–867. DOI: 10.1364/JOSAB.8.000858.

[15] P. B. Corkum. "Plasma perspective on strong field multiphoton ionization".
In: *Phys. Rev. Lett.* 71 (13 Sept. 1993), pp. 1994–1997. DOI: 10.1103/PhysRevLett.71.1994.

[16] H. Wikmark.
Spatial and temporal aspects of intense attosecond pulses for pump-probe experiments.
PhD thesis, Department of Physics, Lund University, 2019.

[17] J. L. Krause, K. J. Schafer, and K. C. Kulander.
"High-order harmonic generation from atoms and ions in the high intensity regime".
In: *Phys. Rev. Lett.* 68 (24 June 1992), pp. 3535–3538. DOI: 10.1103/PhysRevLett.68.3535.

[18] Y. Mairesse et al. "Attosecond Synchronization of High-Harmonic Soft X-rays".
In: *Science* 302.5650 (2003), pp. 1540–1543. ISSN: 0036-8075. DOI: 10.1126/science.1090277.

[19] K. Klünder et al. "Probing Single-Photon Ionization on the Attosecond Time Scale".
In: *Phys. Rev. Lett.* 106 (14 Apr. 2011), p. 143002. DOI: 10.1103/PhysRevLett.106.143002.

[20] J. Rothhardt et al. "Absorption-limited and phase-matched high harmonic generation in the tight focusing regime". In: *New Journal of Physics* 16.3 (Mar. 2014).
DOI: 10.1088/1367-2630/16/3/033022.

[21] J. Schwiegerling and D. R. Neal.
"Historical development of the Shack-Hartmann wavefront sensor".
In: *Robert Shannon and Roland Shack: Legends in Applied Optics, edited by JE Harvey and RB Hooker—SPIE, Bellingham, WA* (2005), pp. 132–139.

[22] J. Y. Wang and D. E. Silva. "Wave-front interpretation with Zernike polynomials".
In: *Appl. Opt.* 19.9 (May 1980), pp. 1510–1518. DOI: 10.1364/AO.19.001510.

[23] U. Even. "The Even-Lavie valve as a source for high intensity supersonic beam".
In: *EPJ Techniques and Instrumentation* 2.1 (2015), p. 17.

[24] F. Campi et al. "Design and test of a broadband split-and-delay unit for attosecond XUV-XUV pump-probe experiments". In: *Review of Scientific Instruments* 87.2 (2016).

[25] H. Wolter. "Spiegelsysteme streifenden Einfalls als abbildende Optiken für Röntgenstrahlen".
In: *Annalen der Physik* 445.1-2 (1952), pp. 94–114. DOI: 10.1002/andp.19524450108.

[26] H. Coudert-Alteirac et al.
"Micro-focusing of broadband high-order harmonic radiation by a double toroidal mirror".
In: *Applied Sciences* 7.11 (2017), p. 1159.

[27] H. Coudert-Alteirac. "Spatial and temporal metrology of intense attosecond pulses".
PhD thesis. Lund University, 2018.

[28] J. Lahl. *Investigation of Ultrafast Molecular Dynamics via Covariance Mapping : A Tool for Intense XUV Light Sources.* PhD thesis, Department of Physics, Lund University, 2019.

[29] M. J. Vrakking. "An iterative procedure for the inversion of two-dimensional ion/photoelectron imaging experiments".
In: *Review of Scientific Instruments* 72.11 (2001), pp. 4084–4089.